

Staphylococcus aureus FtsZ and PBP4 bind to the conformationally dynamic N-terminal domain of GpsB

Michael D Sacco^{1†}, Lauren R Hammond^{2†}, Radwan E Noor³, Dipanwita Bhattacharya², Lily J McKnight², Jesper J Madsen^{1,4}, Xiujun Zhang¹, Shane G Butler¹, M Trent Kemp¹, Aiden C Jaskolka-Brown¹, Sebastian J Khan², Ioannis Gelis³, Praathees Eswara^{2*}, Yu Chen^{1*}

¹Department of Molecular Medicine, Morsani College of Medicine, University of South Florida, Tampa, United States; ²Department of Molecular Biosciences, University of South Florida, Tampa, United States; ³Department of Chemistry, University of South Florida, Tampa, United States; ⁴Global and Planetary Health, College of Public Health, University of South Florida, Tampa, United States

Abstract In the Firmicutes phylum, GpsB is a membrane associated protein that coordinates peptidoglycan synthesis with cell growth and division. Although GpsB has been studied in several bacteria, the structure, function, and interactome of *Staphylococcus aureus* GpsB is largely uncharacterized. To address this knowledge gap, we solved the crystal structure of the N-terminal domain of *S. aureus* GpsB, which adopts an atypical, asymmetric dimer, and demonstrates major conformational flexibility that can be mapped to a hinge region formed by a three-residue insertion exclusive to *Staphylococci*. When this three-residue insertion is excised, its thermal stability increases, and the mutant no longer produces a previously reported lethal phenotype when overexpressed in *Bacillus subtilis*. In *S. aureus*, we show that these hinge mutants are less functional and speculate that the conformational flexibility imparted by the hinge region may serve as a dynamic switch to fine-tune the function of the GpsB complex and/or to promote interaction with its various partners. Furthermore, we provide the first biochemical, biophysical, and crystallographic evidence that the N-terminal domain of GpsB binds not only PBP4, but also FtsZ, through a conserved recognition motif located on their C-termini, thus coupling peptidoglycan synthesis to cell division. Taken together, the unique structure of *S. aureus* GpsB and its direct interaction with FtsZ/PBP4 provide deeper insight into the central role of GpsB in *S. aureus* cell division.

***For correspondence:**

eswara@usf.edu (PE);
ychen1@usf.edu (YC)

[†]These authors contributed equally to this work

Competing interest: The authors declare that no competing interests exist.

Funding: See page 17

Preprinted: 25 October 2022

Received: 14 December 2022

Accepted: 15 April 2024

Published: 19 April 2024

Reviewing Editor: Jie Xiao, Johns Hopkins University, United States

© Copyright Sacco, Hammond et al. This article is distributed under the terms of the [Creative Commons Attribution License](https://creativecommons.org/licenses/by/4.0/), which permits unrestricted use and redistribution provided that the original author and source are credited.

Editor's evaluation

This valuable work reports a unique N-terminal motif of *Staphylococcus aureus* GpsB, the co-crystal structure of GpsB with the C-terminus of PBP4, and the direct interaction between GpsB and the C-terminus of FtsZ. The evidence supporting these discoveries is convincing, with biochemical and structural characterizations. This study sheds light on the role of GpsB in the cell division of this important pathogen.

Introduction

Bacterial cell division is a dynamic process involving more than a dozen proteins that form a multimeric complex at mid-cell. Collectively known as the divisome, this network of scaffolding proteins and enzymes stimulates peptidoglycan synthesis, constricts the existing membrane, and forms the septal

cell wall (**Mahone and Goley, 2020**). While divisomal proteins may differ among certain clades, most are conserved among all bacteria. Perhaps the most important and well-studied divisomal protein is FtsZ, a bacterial homolog of eukaryotic tubulin. FtsZ marks the division site by forming a 'Z-ring' in association with early-stage divisomal proteins such as FtsA, ZapA, SepF, and EzrA in Gram-positive bacteria (**Gamba et al., 2009; Lutkenhaus et al., 2012**). Late-stage divisomal proteins such as DivIVA, FtsL, DivIB, and various penicillin-binding proteins (PBPs) subsequently assemble to carry out cell division and facilitate the separation and creation of identical daughter cells.

GpsB is a DivIVA-like protein that is highly conserved in Firmicutes (**Halbedel and Lewis, 2019; Hammond et al., 2019**). While GpsB is dispensable, or conditionally essential in most Firmicutes (**Rismondo et al., 2016; Fleurie et al., 2014; Claessen et al., 2008; Tavares et al., 2008**), it was reported to be essential for growth in *Staphylococcus aureus* (**Santiago et al., 2015; Gillaspay, 2006**). However, recent studies indicate that *gpsB* may not be essential, but nevertheless plays a significant role in maintaining *S. aureus* cell morphology (**Sutton et al., 2023; Bartlett et al., 2023; Costa et al., 2023**). In particular, the importance of *S. aureus* GpsB (Sa GpsB) for cell division is underscored by its unique ability to regulate FtsZ polymerization in *S. aureus* (**Eswara et al., 2018**). At this time, GpsB-FtsZ interaction has not been reported in other bacteria. Sa GpsB has also been reported to interact with other cell division proteins such as EzrA (**Steele et al., 2011**), DivIVA (**Bottomley et al., 2017**), and the wall teichoic acids (WTA) biosynthesis/export proteins TarO and TarG (**Kent, 2024; Hammond et al., 2022**).

The interaction of GpsB with PBPs has also been investigated in several bacteria, including *Listeria monocytogenes* (Lm) PBPA1, *Streptococcus pneumoniae* (Sp) PBP2a, and *B. subtilis* (Bs) PBP1 (**Halbedel and Lewis, 2019**). These studies show that GpsB binds to a short, ~5- to 30-residue N-terminal sequence found on the cytosolic region of these bitopic PBPs, referred to as an N-terminal 'mini-domain' (**Rismondo et al., 2016; Cleverley et al., 2019**). Cleverley et al. found PBP mini-domains containing an (S/T)-R-X-X-R-(R/K) motif directly interact with the N-terminal domain of GpsB by forming electrostatic interactions and hydrogen bonds with a shallow, acidic cavity located at the GpsB dimer interface (**Figure 1—figure supplement 1A–C**) **Cleverley et al., 2019**.

While Lm, Sp, and Bs have at least six annotated PBPs (**Kocaoglu et al., 2015; Korsak et al., 2010; Kunst et al., 1997**), there are only four in *S. aureus*: PBP1, PBP2, PBP3, and PBP4 (**Gillaspay, 2006**) - five in methicillin-resistant *S. aureus* (MRSA) which expresses an additional β -lactam insensitive PBP, PBP2a (**Hartman and Tomasz, 1984**). *S. aureus* is further distinguished by its highly cross-linked peptidoglycan and can readily become resistant to β -lactams via PBP4 and the acquisition of PBP2a (**Leski and Tomasz, 2005; Snowden and Perkins, 1990**). It is believed this β -lactam-resistant phenotype relies on WTA assembly, which influences the function and localization of PBP4 and PBP2a (**Atilano et al., 2010**). While PBP2a is a historically recognized element of antibacterial resistance, PBP4 has recently been found to contribute to β -lactam insensitivity (**Chatterjee et al., 2017**). As the sole class C PBP in *S. aureus*, PBP4 bears the fold and architecture of a carboxypeptidase, but uniquely catalyzes both transpeptidase and carboxypeptidase reactions (**Finan et al., 2001; Henze and Berger-Bächi, 1995; Navratna et al., 2010; Wyke et al., 1981**).

In this report, we show that Sa GpsB directly binds to FtsZ and PBP4 through a signature GpsB recognition sequence. Further analysis of the GpsB N-terminal domain reveals unique conformations and innate flexibility that is integral to the function of GpsB. Together, these findings provide insight into the unique role of GpsB in synchronizing FtsZ dynamics with cell wall synthesis during cell division in *S. aureus*.

Results

The crystal structure of Sa GpsB N-terminal domain reveals an atypical asymmetric dimer

The full-length Sa GpsB is a relatively small protein of 114 residues. Its N-terminal domain homodimerizes as a coiled-coil, while its smaller C-terminal domain homotrimerizes, forming a hexamer as the biological unit (**Halbedel and Lewis, 2019; Rismondo et al., 2016; Cleverley et al., 2016**). Using X-ray crystallography, we solved the structure of the N-terminal domain (residues 1–70) of Sa GpsB at 1.95 Å resolution in the P2₁ space group (**Figure 1A; Supplementary file 1**), with four monomers per asymmetric unit forming two dimers (dimers A and B). The overall structure of GpsB is similar to

Figure 1 continued

a symmetric dimer based on the sequence of the domain, indicating the presence of conformational heterogeneity. Backbone and Asn/Gln sidechain amide signals are shown in green and purple respectively. **(D)** Comparison of different GpsB/DivIVA monomers from previously solved structures. Pitch angles were determined by placing a marker atom at the centroid of the beginning, midpoint 'hinge', and end of each helix, then measuring the angle. **(E)** Multisequence alignment of GpsB within select members of the Firmicutes phylum and with *S. aureus* DivIVA. Staphylococci GpsB contain a three-residue insertion that forms the hinge region, either MAD or MNN, depending on the sequence alignment parameters. The two Met residues (four per dimer) of the hinge region are designated with a red *. *Sa* - *S. aureus*, *Sh* - *S. haemolyticus*, *Se* - *S. epidermidis*, *Sp* - *S. pneumoniae*, *Bs* - *B. subtilis*, *Bc* - *B. cereus*, *Lm* - *L. monocytogenes*, *Ef* - *E. faecalis*, DivIVA - *S. aureus* DivIVA.

The online version of this article includes the following figure supplement(s) for figure 1:

Figure supplement 1. Crystal structures of penicillin-binding protein (PBP) mini-domains in complex with the N-terminal domain of their cognate GpsB, published by [Cleverley et al., 2019](#).

Figure supplement 2. ^1H - ^{15}N HSQC identifies conformational heterogeneity within the N-terminal domain of *Sa* GpsB.

Figure supplement 3. Molecular dynamics simulations and homology models of GpsB mutants reveal potential structural origins of GpsB stability and flexibility.

previously determined GpsB orthologs ([Figure 1—figure supplement 1](#); [Rismondo et al., 2016](#); [Cleverley et al., 2019](#)) and retains the same fold of DivIVA ([Oliva et al., 2010](#)), though it shares much less sequence similarity ([Figure 1E](#)). Dimerization of the N-terminal domain is facilitated by a pattern of nonpolar residues every three to four residues, promoting the formation of a hydrophobic core in the coiled-coil. This N-terminal domain is partitioned into three regions: a relatively short α -helix with approximately two turns (residues 10–16), a second longer α -helix (residues 28–70) that forms a coiled-coil, and an amphipathic 10-residue loop (residues 17–27) that links these two helices and intertwines with the adjacent protomer, 'capping' GpsB ([Figure 1B](#)). This loop region is proposed to interact with the inner leaflet of the cell membrane ([Halbedel and Lewis, 2019](#)).

The most unique structural feature of *Sa* GpsB is a hinge forming at the midpoint of its N-terminal domain that causes each protomer to bend, adopting pitch angles (θ) of 137–140° (dimer A) and 156–166° (dimer B). In contrast, GpsB protomers from *Lm*, *Bs*, *Sp*, and *Sa* DivIVA are almost linear ($\theta=167$ – 179°) and practically indistinguishable when superimposed ([Figure 1D](#)). We find that there is a 3-amino acid insertion in the *Sa* GpsB sequence where the helicity is disrupted and that a cluster of four Met residues (Met45, Met48) are interlocked at the dimer interface at this position ([Figure 1B](#); dotted rectangle). These Met residues are only found in *Staphylococci* ([Figure 1E](#)) and take the place of an aromatic Tyr or Phe present in other orthologs, which normally stabilize the core via π stacking interactions. While the 3-amino acid insertion likely disrupts the continuity of the coiled-coil, methionine is one of the most flexible aliphatic amino acids and may further contribute to the conformational flexibility.

Experiments using solution state NMR spectroscopy further support the notion of intrinsic conformational heterogeneity, suggesting it is a bona fide structural feature rather than a crystallization artifact. The *Sa* GpsB^{WT}₁₋₇₀ construct contains a two-residue N-terminal extension (GH) after removal of the purification tag, and thus a total of 72 signals are expected. The 2D ^1H - ^{15}N HSQC spectrum shows good signal dispersion ([Figure 1C](#)), which is characteristic of a folded domain. However, a total of 100 well-resolved backbone amide signals are observed, and seven pairs of signals are detected in the Asn/Gln sidechain region instead of four pairs ([Figure 1C](#), [Figure 1—figure supplement 2B](#)). The appearance of the additional signals is not due to proline *cis/trans* isomerization since there are no prolines in the sequence, nor is it due to self-aggregation of the dimers to form a dimer-of-dimers or higher order oligomers, because raising the concentration from 160 to 700 μM has no effect on the number of signals in the spectrum ([Figure 1—figure supplement 2B](#)). In addition, the ^1H - ^{15}N HSQC of *Sa* GpsB^{WT}₁₋₇₀ exhibits differential linewidths, with a set of 13 narrow signals at the center of the spectrum where disordered segments appear, and a larger set of 87 signals dispersed throughout the spectrum. The number of the narrow signals corresponds well with the number of residues found at the flexible N-terminus, suggesting that the appearance of extra signals is due to sampling of multiple conformations of the coiled-coil. Furthermore, three of the four Asn/Gln sidechain pairs showing chemical shift degeneracy are adjacent to the hinge ([Figure 1—figure supplement 2A](#)) providing strong evidence that the observed conformational heterogeneity occurs at this region.

Molecular dynamics (MD) simulations using Gromacs v. 5.0.4 and a CHARMM36m force field also support the idea that conformational flexibility exists in solution. After approximately 100 ns, dimer

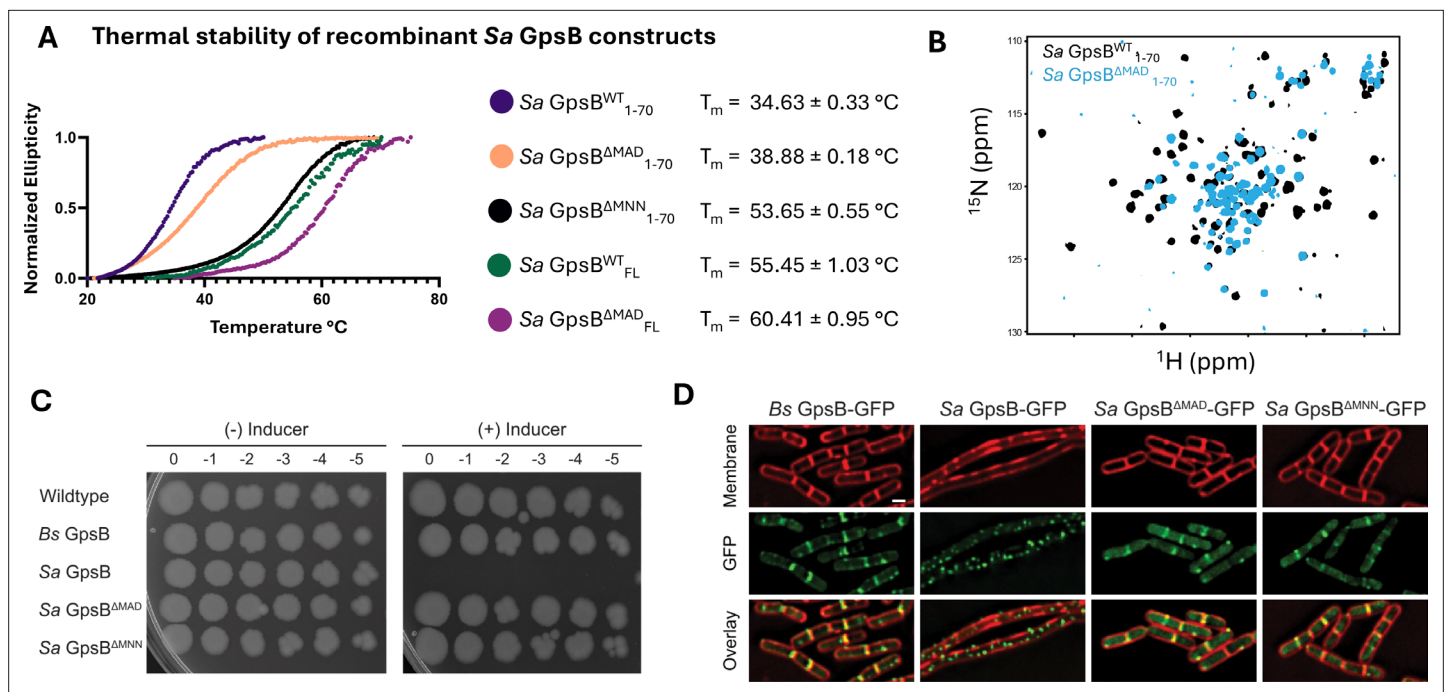


Figure 2. Deletion of a three-residue insertion in *Sa* GpsB increases thermal stability in solution and abolishes toxicity in *B. subtilis*. **(A)** Circular dichroism (CD) melt profiles of recombinantly expressed *Sa* GpsB constructs reveal Δ MAD and Δ MNN mutants have increased T_m , compared to wildtype (WT) *Sa* GpsB. **(B)** Overlays of the ^1H - ^{15}N HSQC of spectrum of *Sa* GpsB^{WT}₁₋₇₀ and *Sa* GpsB^{ΔMAD}₁₋₇₀ suggest there are significant differences in the conformational properties of these two proteins. **(C)** Serial dilutions of *B. subtilis* strains harboring inducible *Bs* GpsB (GG18), *Sa* GpsB (GG7), *Sa* GpsB Δ MAD (LH119), and *Sa* GpsB Δ MNN (LH115), plated on LB plates without (left) and with (right) 1 mM IPTG demonstrate WT *Sa* GpsB is lethal, but Δ MAD *Sa* GpsB and Δ MNN *Sa* GpsB are not. **(D)** Fluorescence micrographs showing the protein localization of *Bs* GpsB-GFP (GG19), *Sa* GpsB-GFP (GG8), *Sa* GpsB-GFP Δ MAD (LH126), and *Sa* GpsB-GFP Δ MNN (LH116). Cell membrane was visualized using SynaptoRed membrane dye (1 $\mu\text{g}/\text{mL}$). Scale bar, 1 μm . In contrast to WT *Sa* GpsB, strains of *B. subtilis* that overexpress Δ MAD and Δ MNN *Sa* GpsB have similar cellular morphology to WT *B. subtilis* and these proteins localize to the division septum.

The online version of this article includes the following source data and figure supplement(s) for figure 2:

Figure supplement 1. Deletion of MNN residues more drastically affects the function of *Sa* GpsB than deletion of MAD residues.

Figure supplement 1—source data 1. Images of total protein gel and anti-GpsB western blot.

Figure supplement 2. Deletion of MAD/MNN residues renders *Sa* GpsB less functional, but only minimally affects the function of heterocomplex with unmutated counterpart.

Figure supplement 2—source data 1. Images of total protein gel and anti-GpsB western blot.

1 adopts an $\sim 180^\circ$ pitch angle that occurs concomitantly to major fluctuations in dimer 2 in a separate simulation (**Figure 1—figure supplement 3A**), although the preference for continuous helical structures (corresponding to $\sim 180^\circ$ pitch angles) may sometimes be influenced by specific force field parameters.

A three-residue insertion unique to *Staphylococci* GpsB disrupts the coiled-coil pattern and destabilizes the structure of *Sa* GpsB

A unique element of *Sa* GpsB that likely contributes to its distinct conformational flexibility are three extra residues located at the hinge region - MAD or MNN (depending on the alignment parameters; **Figure 1E**), roughly corresponding to an extra turn in the helix. Deleting either MAD or MNN produces a homology model where residues 45–70, normally displaced by one turn, are now aligned with their orthologous residue pair (**Figure 1—figure supplement 3B**). To investigate the relative degree of stability imparted by these residues, GpsB mutant lacking the extra MAD or MNN residues at the hinge region was recombinantly constructed and purified, and T_m (melting temperature) was determined using circular dichroism (CD) spectroscopy (**Figure 2A**). This experiment shows the Δ MAD and Δ MNN GpsB have superior thermal stability to wildtype (WT) *Sa* GpsB for both the N-terminal

domain (1–70) and full-length constructs. Perhaps the most notable finding from this experiment was that, while the T_m of Sa GpsB $^{\Delta MAD}_{1-70}$ ($38.88 \pm 0.18^\circ\text{C}$) was only modestly higher than Sa GpsB $^{WT}_{1-70}$ ($34.63 \pm 0.33^\circ\text{C}$), the T_m of Sa GpsB $^{\Delta MNN}_{1-70}$ ($53.65 \pm 0.55^\circ\text{C}$) was highly stable, approximately 1.5-fold higher than that of Sa GpsB $^{WT}_{1-70}$ and comparable to the thermal stability of the full-length Sa GpsB $^{WT}_{FL}$. Though the full-length Sa GpsB $^{\Delta MNN}_{FL}$ was not analyzed, we expect that its T_m would be higher than both Sa GpsB $^{WT}_{FL}$ and Sa GpsB $^{\Delta MAD}_{FL}$ based on the experiments assessing the 1–70 constructs.

The conformational properties of the Sa GpsB $^{\Delta MAD}_{1-70}$ mutant were also different when analyzed by ^1H - ^{15}N HSQC (**Figure 2B**). Most of the dispersed signals from the coiled-coil region experience severe broadening, in many cases beyond detection, as well as changes in chemical shift, while all narrow signals at the center of the spectrum show no change in linewidth or positions. Signal broadening is caused by changes in the rate of interconversion between the available conformations from the intermediate-slow for WT (s) to the intermediate-fast exchange regime for ΔMAD (ms), but without altering the overall number of states, as seven pairs of Asn/Gln sidechain pairs of signals are observed. Conformational rigidity is a well-established correlate of thermal stability (**Karshikoff et al., 2015**), and may contribute to the enhanced T_m of Sa GpsB $^{\Delta MNN}$ and Sa GpsB $^{\Delta MAD}$. The aforementioned homology model (**Figure 1—figure supplement 3B**) corresponding to Sa GpsB $^{\Delta MNN}$ and Sa GpsB $^{\Delta MAD}$ reveals several residues potentially form stronger interactions than the WT. These include an intra-helical electrostatic interaction that replaces a potential repulsion between Asp47 and Glu51 with Asn47/Lys51 in Sa GpsB $^{\Delta MAD}$ and Asp47/Lys51 in Sa GpsB $^{\Delta MNN}$ (**Figure 1—figure supplement 3C**). The favorable Asp47/Lys51 electrostatic interactions in GpsB $^{\Delta MNN}$ may further contribute to its higher thermostability.

The MAD/MNN insertion is critical for GpsB function

Previously, we reported that overproduction of Sa GpsB in *B. subtilis* causes cell division arrest which eventually leads to filamentation and cell lysis (**Eswara et al., 2018**). We used this system to probe the significance of the flexibility provided by MAD/MNN residues for the function of GpsB. First, we conducted a growth assay on solid medium by spotting serial dilutions of cells of *B. subtilis* WT and cells harboring an inducible copy of *Bs gpsB*, *Sa gpsB*, *Sa gpsB^{\Delta MAD}, or *Sa gpsB^{\Delta MNN}. As previously established, overproduction of *Bs GpsB* is not lethal, but Sa GpsB is (**Figure 2C; Eswara et al., 2018; Hammond et al., 2022**). In contrast, overproduction of either ΔMAD or ΔMNN Sa GpsB is not lethal and cells grow as well as the negative controls (*B. subtilis* WT and inducible *Bs GpsB* strain). These results suggest the hinge region of Sa GpsB, characterized by two Met residues (**Figure 1B**), is essential for the normal function of Sa GpsB as assessed by lethal phenotype in *B. subtilis*. To further investigate the impact of these mutations, we examined GFP tagged ΔMAD and ΔMNN Sa GpsB in *B. subtilis* using high-resolution fluorescence microscopy. As reported previously, and as shown in **Figure 2D**, *Bs GpsB*-GFP localizes to the division site (**Claessen et al., 2008; Tavares et al., 2008; Hammond et al., 2022**) and does not lead to filamentation upon overproduction ($2.09 \pm 0.49 \mu\text{m}$; $n=50$), but Sa GpsB-GFP forms foci throughout the entire cell, and causes severe filamentation ($22.83 \pm 16.51 \mu\text{m}$; $n=21$) (**Eswara et al., 2018**). However, ΔMAD and ΔMNN variants of Sa GpsB-GFP do not cause filamentation ($2.13 \pm 0.44 \mu\text{m}$ and $2.10 \pm 0.43 \mu\text{m}$ respectively; $n=50$) and are clearly localized at the division site. It has been noted previously that Sa GpsB-GFP also localizes to the division sites at initial stages prior to causing filamentation at a lower inducer concentration (**Eswara et al., 2018**). Taken together, this data suggests the ΔMAD and ΔMNN mutants presumably interact with the *B. subtilis* cell division machinery to allow for division site localization, but fail to elicit lethal filamentation and toxicity (**Eswara et al., 2018**).**

We also investigated the phenotypes of *S. aureus* strains that overexpress Sa GpsB $^{\Delta MAD}$ and Sa GpsB $^{\Delta MNN}$. First, we conducted a growth assay by spotting serial dilutions of *S. aureus* strains harboring an empty vector (EV) or an additional plasmid-based inducible copy of *Sa gpsB*, *Sa gpsB^{\Delta MAD}, or *Sa gpsB^{\Delta MNN}. Overproduction of Sa GpsB leads to a 100- to 1000-fold growth inhibition compared to EV control (**Figure 2—figure supplement 1A**). Interestingly, while cells overproducing Sa GpsB $^{\Delta MNN}$ grew similarly to the EV control, *Sa gpsB^{\Delta MAD} overexpression resulted in growth inhibition comparable to Sa GpsB. We hypothesized that the difference in phenotype is due to differential affinity of native Sa GpsB (produced from chromosomal locus) to Sa GpsB $^{\Delta MAD}$ and Sa GpsB $^{\Delta MNN}$ mutants (produced from a plasmid-based system), leading to varying propensity for homo/hetero complex formation. To test this, we conducted bacterial two-hybrid analysis in MacConkey plates and liquid culture as reported***

previously (Hammond et al., 2022; Battesti and Bouveret, 2012). As shown in **Figure 2—figure supplement 1B**, the affinity of Sa GpsB^{ΔMNN} to itself appears to be greater compared to Sa GpsB^{ΔMAD} and Sa GpsB. Sa GpsB^{ΔMAD} appears to have similar affinity to itself and Sa GpsB, but it is weaker compared to the self-interaction of Sa GpsB. Thus, the differential affinity between mutant Sa GpsB and WT Sa GpsB could underlie the observed difference in phenotypes. Next, we analyzed the cell morphology of *S. aureus* strains overproducing ΔMAD/ΔMNN mutants. As we have previously shown, overproduction of Sa GpsB leads to cell size enlargement due to cell division inhibition (Eswara et al., 2018). Using fluorescence microscopy (**Figure 2—figure supplement 1C and D**), we re-confirmed the increase in cell diameter in cells overproducing Sa GpsB (1.00 ± 0.19 μm) when compared to the EV control (0.90 ± 0.13 μm). In agreement with the lethal plate phenotype (**Figure 2—figure supplement 1A**), cells overproducing Sa GpsB^{ΔMAD} also displayed a statistically significant increase in cell diameter (0.95 ± 0.16 μm), while Sa GpsB^{ΔMNN} did not (0.91 ± 0.15 μm) and resembled EV control. We also ensured the stable production of Sa GpsB, ΔMAD, and ΔMNN via western blotting (**Figure 2—figure supplement 1E**). Lastly, by GFP tagging, we observed that both mutants localize to the division site similar to Sa GpsB-GFP (**Figure 2—figure supplement 1F**; Eswara et al., 2018; Hammond et al., 2022). In summary, ΔMNN is less functional compared to ΔMAD in terms of causing growth inhibition on plate and cell enlargement phenotype, however both ΔMAD and ΔMNN mutants are able to localize to division sites.

To further test the functionality of the hinge region mutants, we generated a Sa *gpsB* knockout strain using CRISPR/Cas9-based approach (Chen et al., 2017). As the sole copy, Sa *gpsB*^{ΔMAD} appears to be less toxic compared to the inducible WT Sa *gpsB*, suggesting that it is partially functional (**Figure 2—figure supplement 2A**). However, the ability of Sa *gpsB*^{ΔMNN} to impact *S. aureus* growth is severely impaired and resembles the EV control. This observation was consistent with the cell diameter quantification of different strains (**Figure 2—figure supplement 2B**). We also ensured the stability of these mutants is unaffected via western blotting (**Figure 2—figure supplement 2C**). To probe whether these mutants inhibit the native function of Sa GpsB when in a heteromer, similar to other previously isolated and functionally defective Sa GpsB mutants (such as Sa *gpsB*^{ΔLEE}) (Hammond et al., 2022), we co-expressed Sa *gpsB-gfp* and Sa *gpsB*, Sa *gpsB*^{ΔMAD}, or Sa *gpsB*^{ΔMNN} in *B. subtilis*. We observed that co-expression of hinge region mutants does not completely abolish the toxicity of Sa *gpsB-gfp* (**Figure 2—figure supplement 2D**). This result suggests that, although the Sa *gpsB*^{ΔMAD} and Sa *gpsB*^{ΔMNN} mutants are by themselves nonfunctional in *B. subtilis* (**Figure 2C**), they do not drastically inhibit the function of WT GpsB in the heteromer. We hypothesize that the deletion mutants lacking the flexible hinge region may to some degree potentially mimic certain GpsB conformations with varied activities. Thus the new data may indicate that the protomers adopting different conformations within the GpsB complex can function independently of one another, providing a mechanism to fine-tune the function of the whole complex.

The C-terminus of Sa FtsZ binds to the N-terminal domain of Sa GpsB through a conserved (S/T/N)-R-X-X-R-(R/K) motif

One of the few proteins known to interact with Sa GpsB is the tubulin-like GTPase, FtsZ - a central cell division protein that marks the division site in nearly all bacteria. We previously demonstrated that GpsB directly interacts with Sa FtsZ to stimulate its GTPase activity and modulate its polymerization characteristics (Eswara et al., 2018). However, the molecular basis for this interaction was not known. Remarkably, we discovered that the last 12 residues of Sa FtsZ (N-R-E-E-R-R—S-R-R-T-R-R), also known as the C-terminal variable (CTV) region (Buske and Levin, 2012), are a repeated match of the consensus GpsB-binding motif (S/T-R-X-X-R-(R/K)) found in the N-termini of *Bs* PBP1, *Lm* PBPA1, and *Sp* PBP2a. In this instance, the first motif bears an Asn instead of a Ser/Thr. Given the similar physicochemical properties of Asn as a small polar amino acid, it can likely replace Ser or Thr without any functional significance. To our knowledge, the interaction between GpsB and FtsZ is unique to *S. aureus* (Hammond et al., 2019), which is consistent with the absence of this motif in FtsZ orthologs from other organisms (**Figure 3A**).

To initially test whether the predicted FtsZ GpsB-binding motif directly binds to Sa GpsB, we purified and titrated the terminal 66 residues of Sa FtsZ (325–390) against full-length Sa GpsB using surface plasmon resonance (SPR), revealing a dose-dependent interaction ($K_D = 40.21 \pm 1.77 \mu\text{M}$; **Figure 3B**). A simultaneous titration against only the Sa GpsB N-terminal domain (1–70) demonstrates

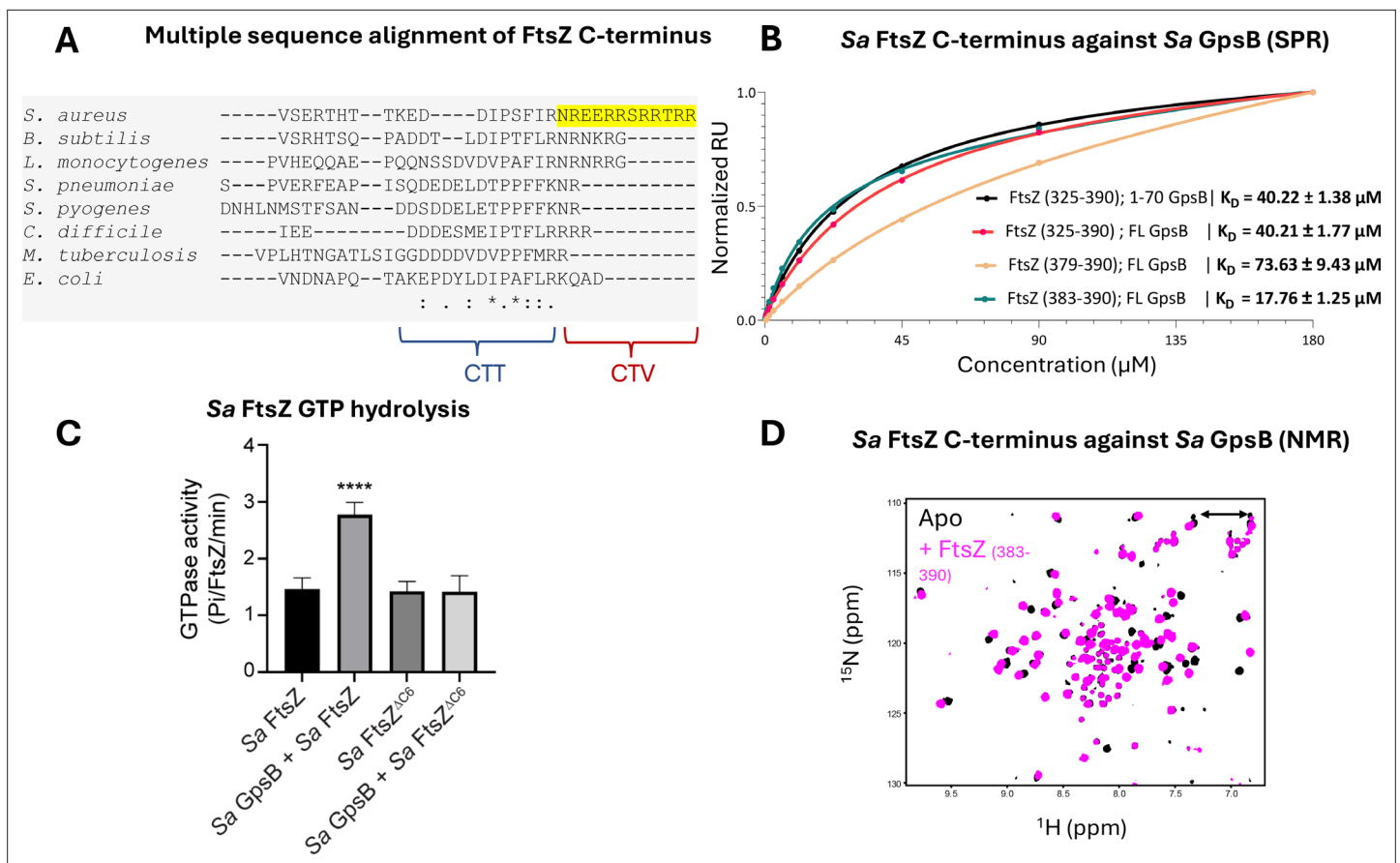


Figure 3. Sa FtsZ contains a repeated GpsB recognition motif at its C-terminus. **(A)** A multiple sequence alignment of the FtsZ C-terminus from different representative bacteria reveals that there is a repeated GpsB recognition motif in Sa FtsZ (highlighted region) and that it is unique to this bacterium. **(B)** Surface plasmon resonance (SPR) titration of peptides corresponding to several segments of Sa FtsZ against Sa GpsB (residues 1–70 or full length). A titration of Sa FtsZ (residues 325–390) against 1–70 GpsB (black), corresponding to the N-terminal domain, shows binding that can be isolated to this region. **(C)** When incubated with Sa GpsB, a Sa FtsZ mutant with a C-terminal truncation (SRRTTR, FtsZ^{ΔC6}) has significantly lower GTP hydrolysis compared to its full-length counterpart. GTP hydrolysis was measured by monitoring inorganic phosphate (P_i) released (μmoles/min) by either FtsZ or FtsZ^{ΔC6} (30 μM) in the absence and presence of GpsB (10 μM). The plot is the average of n=6 independent data sets. p-Value for **** is <0.0001. **(D)** Overlays of the ¹H-¹⁵N HSQC of spectrum of Sa GpsB (1–70) in the absence (black) and in the presence of FtsZ (383–390; pink). The boxed region highlights the only sidechain pair of signals that becomes affected by the addition of Ftsz. Based on a model derived from the structure of Bs GpsB in complex with a penicillin-binding protein (PBP)-derived peptide (**Figure 1—figure supplement 2**), it is tentatively assigned to Q43 of Sa GpsB.

that the C-terminus of Sa FtsZ binds exclusively to this domain ($K_D = 40.22 \pm 1.38 \mu\text{M}$). This is further supported by assays with Sa FtsZ CTV (379–390; $K_D = 73.63 \pm 9.43 \mu\text{M}$) and the final eight residues of Sa FtsZ (383–390; $K_D = 17.76 \pm 1.25 \mu\text{M}$). The described biophysical affinity aligns with previous cellular studies (**Cleverley et al., 2019**), and is consistent with our hypothesis that the impetus for binding is the (S/T/N)-R-X-X-R-(R/K) motif which associates with the PBP-binding pocket (**Figure 1—figure supplement 1**). Unlike the previously identified GpsB-binding motifs located at the N-termini of PBPs, this is the first time such a motif has been found at the C-terminus of a GpsB-binding protein. The approximate fourfold difference in affinity between the CTV and the final eight residues could be a result of the inclusion of two Glu residues in the CTV (E381, E382), which may experience repulsion from the negatively charged PBP-binding pocket of GpsB. Notably, the GpsB recognition motif of Sa FtsZ is adjacent to the C-terminus carboxylate, which imparts an additional negative charge.

To further characterize the interaction between Sa FtsZ and Sa GpsB, we conducted a GTPase assay with Sa GpsB and Sa FtsZ or Sa FtsZ with the C-terminal six residues truncated (Sa FtsZ^{ΔC6}). Briefly, in our previous report (**Eswara et al., 2018**), we found that Sa GpsB enhances the GTPase activity of Sa FtsZ. Therefore, we hypothesized that truncation of the terminal six residues of Sa FtsZ would eliminate the GpsB-mediated enhancement of GTPase activity. As shown in **Figure 3C**, and as

reported previously, addition of Sa GpsB enhanced the GTPase activity of Sa FtsZ. However, this effect was not seen in Sa FtsZ^{ΔC6}, suggesting that the last six C-terminal residues of Sa FtsZ is likely where the interaction with Sa GpsB occurs.

The interaction of the Sa GpsB N-terminal domain with the Sa FtsZ derived peptide (383–390) was also monitored using NMR (**Figure 3D**). Addition of the octapeptide to ¹⁵N-labeled N-terminal domain results in a significant chemical shift perturbation to a small number of dispersed signals in the ¹H-¹⁵N HSQC spectrum, suggesting that the interaction is highly localized and occurs through the coiled-coil region without disturbing the conformational heterogeneity of the dimer. The available structures of Bs GpsB and Sp GpsB in complex with PBP-derived peptides (**Figure 1—figure supplement 1A–C**) suggest the complex is stabilized through interactions with helices 1 and 2, as well as part of the h1-h2 capping loop (**Cleverley et al., 2019**). The N-terminal Arg of Sa FtsZ octapeptide utilized in our experiments is expected to be placed in the PBP-binding pocket near Q43, based on the complex structures of GpsB homologs. Indeed, only one of the Asn/Gln pairs of signals in the ¹H-¹⁵N HSQC is shifted upon addition of the peptide, while in agreement with our model all other sidechain signals lie far from the binding site (**Figure 1—figure supplement 2A and B**), suggesting that Sa GpsB recognizes partner proteins in a conserved manner.

The cytosolic, C-terminal mini-domain of Sa PBP4 binds to Sa GpsB through its (S/T/N)-R-X-X-R-(R/K) recognition motif

S. aureus has an unusually low number of PBPs in its genome (**Gillaspy, 2006**). Although PBP1, PBP2, PBP2a, and PBP3 all have a cytoplasmic N-terminal ‘mini-domain’, none bear a GpsB recognition motif (**Figure 4A**). Using SPR, we confirmed their cytoplasmic mini-domains have no affinity for Sa GpsB, which is in agreement with the findings from previous bacterial two-hybrid assays (**Steele et al., 2011**). Remarkably, PBP4, the only class C PBP encoded in the *S. aureus* genome, which purportedly functions as both a carboxypeptidase and transpeptidase PBP (**Maya-Martinez et al., 2018**), has a short, cytosolic C-terminal mini-domain with the sequence of N-R-L-F-R-K-R-K, satisfying the consensus GpsB-binding motif (S/T/N)-R-X-X-R-(R/K) found in *S. aureus* FtsZ and in orthologous PBPs found to bind to GpsB. Next, using SPR, we demonstrate this Sa PBP4 C-terminal octapeptide binds to Sa GpsB with a K_D of $48.61 \pm 1.86 \mu\text{M}$ (**Figure 4A**). Supporting this finding is a potential interaction between Sa PBP4 and Sa GpsB previously noted in a bacterial two-hybrid study (**Kent, 2024**).

Initial efforts to obtain a crystal structure of Sa PBP4 and Sa FtsZ with Sa GpsB were unsuccessful. A key factor preventing the formation of this complex were the tight interactions forming at the crystal packing interface. By extending the asymmetric unit, we found each GpsB dimer coordinates two others in a head-to-head arrangement (**Figure 4—figure supplement 1A and B**). This involves the insertion of Arg and Lys residues from the membrane-binding loop into the PBP-binding site from the adjacent GpsB protomer, mimicking the binding mode observed between PBP mini-domains and GpsB in orthologous structures, such as Bs PBP1 (**Figure 4—figure supplement 1C and D**; **Cleverley et al., 2019**). It is unclear whether this head-to-head interaction occurs in the cell or is simply a crystallization artifact. Nonetheless, it is apparent this interaction would need to be disrupted to capture interactions with a binding partner. To do so, we generated an R24A mutant because of its central role in the head-to-head interaction and its distance from the PBP-binding groove. This point mutation successfully disrupted the occluded crystal packing interface and allowed us to determine a 2.40 Å resolution structure of Sa PBP4 peptide bound to Sa GpsB (**Figure 4B, Supplementary file 1**). Unambiguous electron density for the Sa PBP4 C-terminal octapeptide, which adopted an α -helix, was resolved at the PBP-binding groove of GpsB. This structure clearly shows that two of these residues, Arg425 and Arg428, are key components of the Sa PBP4-Sa GpsB interaction, where they form multiple hydrogen bonds with the main chain amides of Sa GpsB Ile13, Tyr14, Lys16, and the sidechain hydroxyl of Tyr26. Furthermore, Arg425 and Arg428 form two salt bridges with the carboxyl sidechain of Asp32. Additionally, Sa GpsB Asp36 appears to play a major role in stabilizing the PBP4 α -helix by forming two hydrogen bonds with the backbone nitrogen of Arg425 and Leu426, an arrangement that is only possible when these two residues are part of an α -helix. Overall, the complex of Sa PBP4/Sa GpsB is very similar to Bs PBP1/Bs GpsB (**Figure 1—figure supplement 1, Figure 4—figure supplement 1C and D**) and is distinguished by the interactions of two Arg residues with the backbone and acidic sidechains lining the PBP-binding groove. We further used AlphaFold2-Multimer to study the interactions between Sa GpsB and FtsZ (**Evans et al., 2021**). Although attempts using full-length

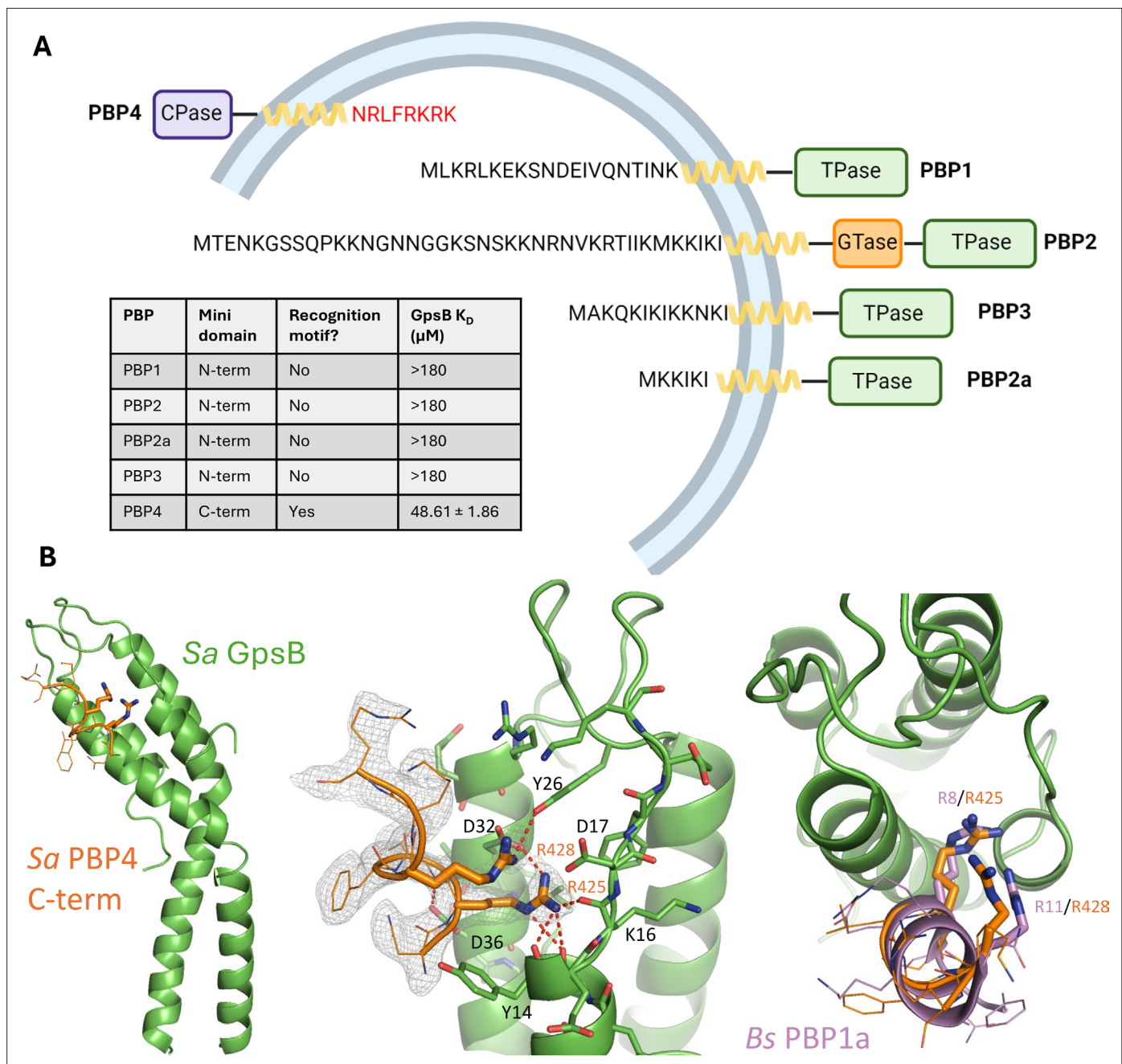


Figure 4. The C-terminal mini-domain of PBP4 directly interacts with GpsB. **(A)** Domain representation of the four/five *S. aureus* (COL)/methicillin-resistant *S. aureus* (MRSA) (USA300) penicillin-binding proteins (PBPs). Each protein is shown from the N-terminus (left) to the C-terminus (right). All four transpeptidase PBPs - PBP1, PBP2, PBP3, and PBP2a - lack a GpsB recognition motif on their N-terminal, cytosolic mini-domain. In contrast, the C-terminal mini-domain of PBP4, the sole *S. aureus* class C PBP, contains this motif (NRLFRKRK, red). The dissociation constants were determined with SPR ($n=2$). **(B)** Crystal structure of Sa GpsB R24A in complex with PBP4 C-terminal peptide fragment at 2.40 Å resolution. The middle panel includes the electron density map of the Sa PBP4 heptapeptide, $2F_o - F_c = 1.0\sigma$. The right panel shows a superimposition of the Bs PBP1 mini-domain from the Bs GpsB+PBP1 complex (PDB ID 6GP7, purple) highlighting similar binding features.

The online version of this article includes the following figure supplement(s) for figure 4:

Figure supplement 1. The crystal packing interface of Sa GpsB dimers form interactions that mimic those between GpsB-PBP pairs.

Figure supplement 2. Surface plasmon resonance (SPR) titration of Sa FtsZ C-terminal peptides against Sa GpsB^{ΔMAD}_{FL}.

Figure supplement 3. AlphaFold2-Multimer prediction of GpsB:FtsZ³⁸⁵⁻³⁹⁰ complex (cyan) superimposed onto the GpsB:PBP4 peptide crystal structure (green:orange).

GpsB and/or long segments of the FtsZ C-terminal domain did not provide satisfying results, a model with the last six residues (S-R-R-T-R-R) was obtained and the nature of interaction resembles the *Sa* GpsB complex structure with the PBP4 peptide (**Figure 4—figure supplement 3**).

Sa FtsZ and Sa PBP4 have lower affinity for Sa GpsB^{ΔMAD}_{FL} compared to Sa GpsB^{WT}_{FL}

Due to the apparent importance of the three-residue insertion at the midpoint of *Sa* GpsB, we also tested the affinity of *Sa* FtsZ and *Sa* PBP4 derived peptides against *Sa* GpsB^{ΔMAD}_{FL}. Using SPR we found that the affinity was significantly reduced for *Sa* GpsB^{ΔMAD}_{FL} compared to *Sa* GpsB^{WT}_{FL} (**Figure 4—figure supplement 2, Supplementary file 2**). Dose-dependent saturation was very weak ($K_D > 200 \mu\text{M}$) for *Sa* PBP4 (423–431) and *Sa* FtsZ (379–390), which verged on being undetectable. Additionally, titration of ¹⁵N-labeled *Sa* GpsB^{ΔMAD}₁₋₇₀ with the *Sa* FtsZ₃₈₃₋₃₉₀ peptide does not result in chemical shift changes to the GpsB^{ΔMAD} ¹H-¹⁵N HSQC, but only in broadening of a small number of signals, which is consistent with the higher K_D measured by SPR (**Figure 1—figure supplement 2C**). While these mutants demonstrate better thermal stability (**Figure 2A**), it is possible their deletion may disrupt interactions with α -helix 1 (residues 10–16; **Figure 1B**), which may subsequently alter the size or shape of the PBP-binding pocket, thus reducing the favorable interactions that promote binding.

Discussion

GpsB is an important protein that coordinates multiple elements of the cell wall synthesis machinery. Although GpsB is widespread among Firmicutes, it has unique structural characteristics and functional roles in *S. aureus*. In this study, we initially present the crystal structure of the *Sa* GpsB N-terminal domain (1–70) (**Figure 1A**). The characteristic coiled-coil motif demonstrates conformational flexibility resulting from a three-residue hinge region that is unique to *Staphylococci* (**Figure 1C, D, and E**). The function of this hinge region and the flexibility it imparts remains unclear, but its deletion increases thermal stability (**Figure 2A**) and weakens affinity for *Sa* FtsZ and *Sa* PBP4 (**Supplementary file 2**). Furthermore, unlike WT *Sa* GpsB, ΔMAD and ΔMNN mutants are not toxic to *B. subtilis* (**Figure 2C and D**), underscoring the cellular significance of this region. In *S. aureus*, we show that the phenotypes of ΔMAD (but not ΔMNN) mimic those of *Sa* GpsB (**Figure 2—figure supplement 1A and C**). Regardless, both ΔMAD and ΔMNN mutants localize to the division site in both *S. aureus* and *B. subtilis* suggesting they retain some level of affinity for their usual interaction partners. In *S. aureus* ΔgpsB background, ΔMAD and ΔMNN mutants are less functional to varying extent (**Figure 2—figure supplement 2A**). Our analysis through co-expression of ΔMAD or ΔMNN with WT *Sa* GpsB in *B. subtilis* revealed that the heterocomplex is functional (**Figure 2—figure supplement 2D**). Taken together, we believe that the hinge region in *Sa* GpsB may permit the protomers with different conformations within the complex to function independently from each other to allow for the fine-tuning of function and/or protein interactions.

Next, we identified a GpsB recognition motif on the C-termini of both *Sa* FtsZ and *Sa* PBP4, leading to biophysical, biochemical, and structural experiments providing evidence of a direct interaction between these proteins and the N-terminal domain of *Sa* GpsB (**Figure 3**). This recognition motif, which is also present, but in the N-termini of *Lm* PBPA1, *Sp* PBP2a, and *Bs* PBP1, involves the insertion of several Arg residues into the binding groove formed at the coiled-coil interface near the membrane-binding loop (**Figure 1—figure supplement 1; Cleverley et al., 2019**).

Our group previously found that *Sa* GpsB interacts with *Sa* FtsZ to regulate its polymerization characteristics, but the repeated (S/T/N)-R-X-X-R-(R/K) GpsB recognition motif on its C-terminus was not recognized until the work on such motifs in PBPs published by **Cleverley et al., 2019**. This motif is unique to *Staphylococci* FtsZ and is absent/less conserved in other Firmicutes (**Figure 3A**). It is unclear why the GpsB recognition motif is repeated, since there is only enough area in the PBP-binding groove to accommodate a helix of eight to nine residues. It is possible that *Sa* FtsZ binds two *Sa* GpsB dimers simultaneously, given the putative arrangement of GpsB as trimer of dimers (**Cleverley et al., 2016**). Alternatively, the first site may be occluded by the binding of other FtsZ interaction partners that are known to bind FtsZ through the C-term such as FtsA, EzrA, and SepF (**Huang et al., 2013**). This finding, in addition to our previous reports (**Eswara et al., 2018; Hammond et al., 2022**), underscore the importance of GpsB in *S. aureus* cell division.

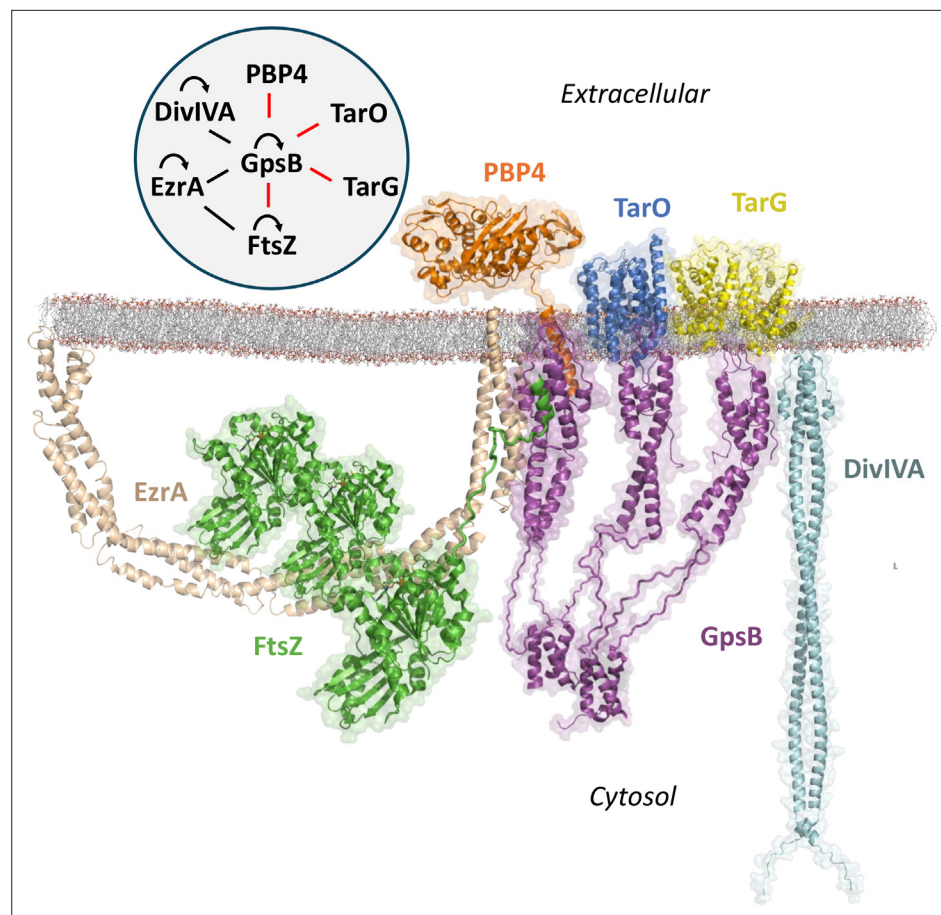


Figure 5. Known interactome of *Sa* GpsB and putative arrangement at the division septum in graphical and diagram (upper left) format. In this paper, we demonstrate that the C-terminal mini-domain of PBP4 (orange) and the C-terminus of FtsZ (green) bind to the N-terminal domain of GpsB (purple). The regions within GpsB responsible for interacting with other partners remain to be elucidated. For interaction diagram, the red lines indicate interactions putatively unique to *S. aureus*, black lines indicate interactions found in both *S. aureus* and *B. subtilis*, and curved arrows represent self-interaction.

A crystal structure of the *Sa* PBP4 C-terminal recognition sequence bound to the N-terminal domain of GpsB reveals a binding mode that mimics previously solved orthologous PBP/GpsB pairs. This discovery is notable because it was previously thought that only the N-terminal ‘mini-domain’ of transpeptidase PBPs (class A, class B) could bind to GpsB. Furthermore, this finding is significant not only because it is the sole *S. aureus* PBP that binds to GpsB, but also because *Sa* PBP4 is intimately associated with WTA synthesis (Atilano *et al.*, 2010; Farha *et al.*, 2013). Previous studies have found that *Sa* GpsB interacts with the WTA biosynthesis pathway proteins TarO (Kent, 2024) and TarG (Hammond *et al.*, 2022), and likely facilitates the export of WTA to the septal cell wall. To our knowledge, *Sa* PBP4 does not directly interact with any of the known WTA machinery. However, it does require WTA for recruitment to the division septum, and impairment of WTA assembly results in delocalization of *Sa* PBP4 (Atilano *et al.*, 2010). Thus, while *Sa* PBP4 itself is not essential for growth, it is tightly regulated by WTA synthesis, an essential process that is also mediated by GpsB (Kent, 2024; Hammond *et al.*, 2022). Thus, it is conceivable that GpsB likely arrives at the division site together with FtsZ, facilitates WTA synthesis, and subsequently recruits PBP4 to promote efficient cytokinesis.

PBP4 joins several other known proteins found to interact with *Sa* GpsB: EzrA (Steele *et al.*, 2011), DivIVA (Bottomley *et al.*, 2017), FtsZ (Eswara *et al.*, 2018), TarO (Kent, 2024), and TarG (Hammond *et al.*, 2022; Figure 5). The interaction diagram outlines the known interactions for GpsB to date but given the diverse number of proteins at the divisome and various binding surfaces on GpsB, it will surely be expanded in the future. Furthermore, while GpsB lacks certain direct interactions with other

known divisome proteins, they are indirectly linked through intermediate proteins. For example, *Sa* FtsZ binds to *Sa* EzrA, a protein known to interact with the SEDS-PBP pairs *Sa* PBP1-FtsW and *Sa* PBP3-RodA, thus indirectly coupling *Sa* GpsB to enzymes that are critical for peptidoglycan synthesis at the divisome (Steele et al., 2011; Reichmann et al., 2019).

When evaluating the biophysical affinity of *Sa* FtsZ and *Sa* PBP4 for *Sa* GpsB, it is important to consider the peptide dissociation constants determined by SPR (~20–80 μ M) may not directly translate to, and likely underestimate, the cellular affinity. The divisome is a highly complex environment with multiple proteins that interact near or at the cell membrane. The enrichment of both *Sa* FtsZ and *Sa* PBP4 at the division septum likely increases their apparent affinity simply based on avidity. Additionally, the arrangement of proteins may introduce synergistic interactions. Studies have found that EzrA, which binds to *Sa* GpsB (Steele et al., 2011), also binds to the C-terminus of FtsZ (Buske and Levin, 2012; Singh et al., 2007), likely upstream of the *Sa* GpsB recognition motif in *S. aureus*. This interaction could both increase the local concentration of *Sa* FtsZ and induce molecular recognition features that promote association with *Sa* GpsB. In addition, the oligomeric state of FtsZ and GpsB may further lead to cooperativity in the interactions between the FtsZ filament and GpsB hexamers. However, tighter binding may also prove deleterious in certain scenarios, especially for dynamic proteins like FtsZ. Given that *Sa* GpsB enhances the GTPase activity (required for FtsZ filament disassembly) of *Sa* FtsZ (Eswara et al., 2018), it is possible GpsB could dynamically promote polymerization and depolymerization of FtsZ.

Under the specter of growing antibacterial resistance, the identification of novel antibiotic targets is becoming increasingly urgent. Beyond PBPs, the bacterial divisome is a largely untapped source of antibiotic targets. The delineation of the physiological role of *Sa* GpsB, identification of its recognition motifs, and characterization of its 3D structure greatly enables modern antibiotic drug-discovery strategies. Furthermore, the involvement of *Sa* GpsB in multiple essential processes presents the opportunity to design targeted antibiotics. There is a growing need for narrow-spectrum antibiotics, especially for common infections, such as those caused by *S. aureus* (Melander et al., 2018). Narrow-spectrum antibiotics avoid selective pressure of commensal bacteria which can serve as a reservoir for resistance elements. In the same vein, their limited disruptive properties can avoid pathologies associated with bacterial dysbiosis, like *Clostridioides difficile* infection. The results from this study provide new information for both understanding the role of GpsB in *S. aureus* division and probing new avenues for narrow-spectrum antibiotic development.

Methods

Recombinant protein cloning and purification

The nucleotide sequence of *Sa* *gpsB* corresponding to the N-terminal domain (1–70) and full length (1–114) was inserted into a modified pET28a vector with a His-TEV sequence 5' to the multiple cloning site (MCS). GpsB constructs expressed for SPR bioanalysis were cloned into a separate pET28a vector with a His-TEV-Avi sequence flanking the MCS (pAViBir). Δ MAD and Δ MNN mutants were generated with QuikChange site-directed mutagenesis using custom primers (Δ MAD (5'-GATTATCAAAAAATGAATAATGAAGTTGAAAATTATCAGAAGAGAATC) and Δ MNN (5'-GATTATCAAAAAATGGCCGATGAAGTTGAAAATTATCAGAAGAG)). All plasmids were transformed into Rosetta (DE3) pLysS cells. A single colony was grown in LB media supplemented with 35 μ g/mL chloramphenicol and 50 μ g/mL kanamycin at 37°C overnight. The overnight culture was then diluted into 1 L LB media at 1:500 and incubated at 37°C until the OD₆₀₀ reached 0.8. Protein expression was initiated with 0.5 mM IPTG and continued incubation at 25°C overnight. pAviBir constructs were biotinylated during IPTG induction with a stock of 5 mM biotin dissolved in bicine for a final concentration of 50 μ M. Cells were harvested by centrifugation at 5000 \times g for 10 min. The cell pellet was resuspended in buffer A (20 mM Tris-HCl pH 8.0, 300 mM NaCl, 20 mM imidazole, and 10% glycerol). Cells were disrupted by sonication followed by centrifugation at 35,000 \times g for 40 min. The pellet containing the protein was resuspended in buffer AD (100 mM Tris-HCl pH 8.0, 6 M guanidine HCl, 300 mM NaCl) and incubated at 30°C for ~1 hr to fully dissolve the pellet, followed by centrifugation at 45,000 \times g for 1 hr. The supernatant was then loaded onto a HisTrap affinity column and eluted in a single step using Buffer BD (100 mM sodium acetate pH 4.5, 6 M guanidine HCl, 300 mM NaCl). The eluted protein was diluted dropwise in refolding buffer (100 mM Tris pH 8.0, 200 mM NaCl) and allowed to refold

overnight at 4°C. The sample was then loaded to a HisTrap column and eluted with linear gradient of imidazole. The fractions containing GpsB were pooled and concentrated. The protein was then incubated with TEV at 1:20 ratio overnight at 4°C. The sample was then loaded onto a HisTrap for reverse Ni²⁺ cleanup. Flow-through was collected and purified using a HiLoad 16/60 Superdex 75 size exclusion column. The protein was stored at -80°C in the storage buffer (20 mM Tris-HCl pH 8.0, 200 mM NaCl). The purity of the protein was determined by SDS-PAGE as >95%. ¹⁵N-labeled GpsB (1-70) for NMR spectroscopy was expressed in the same way, but in minimal media containing ¹⁵N NH₄Cl and ¹²C glucose as the source of nitrogen and carbon, respectively, supplemented with MgSO₄, CaCl₂, and trace metals.

Strain construction

Plasmids were generated using standard cloning procedures. The C-terminal six-residue truncation of FtsZ (FtsZ^{ΔC6}) was generated by PCR using primer pairs oDB9/oDB10 (NdeI/XhoI) and cloned into the pET28a to create pDB1. FtsZ CTT encoding the C-terminal 66 amino acids of *S. aureus* FtsZ was cloned into pET28a using oP228/oP229 (NdeI/BamHI) to create pSK4. These were then transformed into BL21-DE3 cells creating EDB01 and SK7, respectively. ΔMAD was created by using site-directed mutagenesis with custom primers (5'-GATTATCAAAAAATGAATAATGAAGTTGTAAAATTATCAG AAGAGAATC) and ΔMNN was ordered from Integrated DNA Technologies as oLHgblock1. These mutations were then PCR-amplified and cloned into pDR111 to create both untagged (oP36/oP38; Hind111/Sph1) and GFP tagged (oP36/oP37; Hind111/Nhe1 and oP46/oP24; Nhe1/Sph1) variants. Plasmids were then transformed into PY79 and screened for amyE integration resulting in strains LH115, LH116, LH119, and LH126. The PCR products containing the ΔMAD and ΔMNN mutations were also cloned into pCL15 backbone using the same primers and restriction sites to create plasmids pLH62, pLH59, pLH63, and pLH60. These plasmids were then transformed into RN4220 cells resulting in strains LH129, LH127, LH130, and LH128. Then these plasmids were transduced into SH1000 to create strains LH135, LH134, LH133, and LH132. To make the BTH plasmids, ΔMAD and ΔMNN were amplified (BTH11/BTH12; EcoRI/XhoI) and cloned into pEB354 and pEB355 resulting in strains LH164, MA1, LH170, and LH168. The genotypes of strains and oligonucleotides used in this study are provided in **Supplementary files 3 and 4**.

CRISPR/Cas9-based *gpsB* deletion

Plasmid pCAS^{SA} was used to delete *gpsB* from *S. aureus* RN4220 genome (**Chen et al., 2017**). Guide RNA (gRNA) targeting *gpsB* was designed with primer pairs oLM25/26. Primers were phosphorylated via T4 polynucleotide kinase treatment. Following phosphorylation, primers were annealed in the same reaction mixture supplemented with 2.5 μL of 1 M NaCl at 95°C for 3 min. Annealed gRNA was inserted upstream of *cas9* gene via compatible BsaI restriction sites utilized for Golden Gate Assembly. Upstream and downstream regions of *gpsB* were amplified for use in Gibson Assembly. The upstream region was amplified with primer pairs oLM27/28, containing restriction site XbaI compatible with pCAS^{SA} and complementary to downstream sequence. The downstream region was ordered in a geneblock (gLM1 with internal XhoI site corrected) and amplified with primer pairs oLM29/30, containing complementarity to upstream (**Hammond et al., 2022**) sequence and restriction site XhoI compatible with pCAS^{SA}. pCAS^{SA} containing gRNA was digested with XbaI and XhoI for linearization. Gibson Assembly was performed to insert amplified regions downstream of the gRNA scaffold. The resulting plasmid pLM29 was transformed into *Escherichia coli* DH5a. Correct conformation and insertion of sequences was confirmed via Sanger sequencing with primer pair oLM31/32. pLM29 was transformed into RN4220 via electroporation and incubated at 30°C for 24 hr. Colonies were screened with colony PCR for the amplification of *gpsB*. If *gpsB* was not detected, colony PCR was performed and the PCR product amplified using up- and downstream primers of *gpsB* locus was sent for Sanger sequencing to confirm *gpsB* deletion. Knockout strains were plasmid-cured by incubation of strains at 30°C overnight in 3 mL TSB. Overnight cultures were then diluted 1:1000 in TSB and incubated at 42°C until culture grew turbid. Confirmation of successful plasmid curing was determined by verifying susceptibility to 10 μg/mL chloramphenicol. Western blot analysis was also performed on knockout strains using α-GpsB antibody to ensure lack of GpsB production.

X-ray crystallography

Crystals of GpsB (1–70) were grown in a hanging drop apparatus by mixing 11 mg/mL GpsB (purity >98%) with crystallization buffer (30% PEG 3350, 0.4 M NaCl, and 0.1 M Tris pH 8.5) in an equal ratio at 20°C. Filamentous crystals appeared overnight and were harvested after 1 week of growth by briefly transferring to cryoprotectant (30% PEG 3350, 0.4 M NaCl, 0.1 M Tris pH 8.5, and 15% glycerol), followed by flash freezing in liquid nitrogen. GpsB (1–70) and PBP4 (424–451) were mixed in a 1:1 ratio with a GpsB concentration of 6 mg/mL and 1.44 mM PBP4 peptide (1:1 ratio). Initial crystals grew in 25% PEG 4000, 0.1 M Tris pH 8.0, and 0.2 M sodium acetate. These crystals were crushed, diluted 10,000-fold, then seeded into drops in a ratio of 1:1:0.5 (protein, crystallization solution, seed stock). Crystals were harvested after 1 week of growth by transferring to a cryoprotectant solution of 27.5% PEG 4000, 0.1 M Tris pH 8.0, 0.2 M sodium acetate, and 15% glycerol. X-ray diffraction data were collected on the Structural Biology Center (SBC) 19-ID beamline at the Advanced Photon Source (APS) in Argonne, IL, and processed and scaled with the CCP4 versions of iMosflm (Battye *et al.*, 2011) and Aimless (Evans and Murshudov, 2013). Initial models were obtained using the MoRDa (Vagin and Lebedev, 2024) package of the online CCP4 suite. Unmodeled regions were manually built and refined with Coot (Emsley and Cowtan, 2004).

Circular dichroism

Thermal stability was assessed with CD using a Jasco J-815 CD spectropolarimeter coupled to a Peltier cell holder. Recombinantly expressed and purified WT GpsB and GpsB mutants were diluted to 2 µg/mL in 50 mM sodium phosphate (pH 7.0) and CD spectra were measured at 222 nm from 20°C to 80°C. Melting temperature was determined with a 4-parameter logistic curve fit using GraphPad Prism 9.

Surface plasmon resonance

A Series S CM5 chip (Cytiva) was docked into a Biacore S200 instrument (Cytiva) followed by surface activation with NHS/EDC amine coupling. Lyophilized neutravidin (Thermo Fisher Scientific) was dissolved in sodium acetate pH 5.25 to a final concentration of 0.25 mg/mL and injected onto the activated CM5 chip at 10 µL/min for 5 min. Biotinylated GpsB was diluted to 1 mg/mL in HEPES-buffered saline (HBS) and injected over the neutravidin-immobilized CM5 chip at 20 µL/min for 5 min. Synthetic peptides and recombinantly expressed Sa FtsZ (325–390) were serially diluted in HBS, and injected at 30 µL/min for 50 s with a dissociation of 100 s, followed by a stabilization period of 15 s and a buffer wash between injections. All experiments were performed in technical duplicate. Dissociation constants were determined with a one site binding model using GraphPad Prism 9.

NMR spectroscopy

2D ¹H-¹⁵N HSQC spectra of Sa GpsB (1–70) were recorded on an Agilent 800-MHz direct drive instrument equipped with a cryoprobe. NMRpipe (Delaglio *et al.*, 1995) and Sparky (University of California, San Francisco) were used for processing and analysis, respectively. All spectra were acquired in 20 mM Tris pH 8.0, 200 mM NaCl, prepared in 7.5% D₂O, and at 25°C. The concentration of Sa GpsB^{WT}₁₋₇₀ was 160 or 700 µM for the free protein spectrum and 160 µM for the complex with the Sa FtsZ octapeptide, which was added in a 1.5× molar excess.

GTP hydrolysis of FtsZ

Sa FtsZ, Sa GpsB, and Sa FtsZ^{ΔC6} were purified using Ni-NTA affinity chromatography as described previously (Eswara *et al.*, 2018). The effect of GpsB on the GTPase activity of FtsZ and FtsZ^{ΔC6} was determined by measuring the free phosphate released using the malachite green phosphate assay kit (Sigma-Aldrich, MAK307-1KT). Briefly, either FtsZ or FtsZ^{ΔC6} (30 µM) was incubated with GpsB (10 µM) in the polymerization buffer (20 mM HEPES pH 7.5, 140 mM KCl, 5 mM MgCl₂) containing 2 mM GTP at 37°C for 15 min. The free phosphate released was determined by measuring the absorbance of the reaction mixture at 620 nm. Statistical analysis was completed using GraphPad Prism 9 with the one-way ANOVA and post hoc multiple comparisons.

***B. subtilis* and *S. aureus* growth conditions**

Liquid cultures of *B. subtilis* cells were grown in LB and *S. aureus* cells were grown in TSB supplemented with 10 µg/mL chloramphenicol at 37°C.

Spot titer assays

Overnight cultures of *B. subtilis* and *S. aureus* strains were back diluted to OD₆₀₀=0.1 and grown to midlog phase (OD₆₀₀=0.4). Cultures were then back diluted to an OD₆₀₀ of 0.1, serially diluted, and spotted onto LB plates with or without 1 mM IPTG (*B. subtilis*), or TSA plates supplemented with 10 µg/mL chloramphenicol with or without 1 mM IPTG (*S. aureus*), and incubated overnight at 37°C. Spot titers were repeated twice in technical triplicate each time.

Fluorescence microscopy

Overnight cultures of *B. subtilis* and *S. aureus* strains to be imaged were back diluted to OD₆₀₀=0.1 and grown to midlog phase (OD₆₀₀=0.4) and then induced with 1 mM IPTG and allowed to grow for an additional 2 hr. Cells were then prepared and imaged as previously described (**Brzowski et al., 2019**). Briefly, 1 mL aliquots were spun down, washed, and resuspended in PBS. Cells were then stained with 1 µg/mL SynaptoRed fluorescent dye (MilliporeSigma, 574799-5MG) to visualize the membrane and 5 µL of culture was spotted onto a glass bottom dish (Mattek, P35G-1.5-14-C). Images were captured on a DeltaVision Core microscope system (Leica Microsystems) equipped with a Photometrics CoolSnap HQ2 camera and an environmental chamber. Seventeen planes were acquired every 200 nm and the data were deconvolved using SoftWorx software. Cells were measured using ImageJ and analyzed using GraphPad Prism 9 with the one-way ANOVA and post hoc multiple comparisons.

Bacterial two-hybrid assay

Plasmids carrying genes of interest cloned into the pEB354 (T18 subunit) and pEB355 (T25 subunit) backbones were transformed pairwise into BTH101 cells. Overnight cultures of the strains grown in 100 µg/mL ampicillin, 50 µg/mL kanamycin, and 0.5 mM IPTG, at 30°C, were spotted onto MacConkey agar containing 1% maltose that were also supplemented with ampicillin, kanamycin, and IPTG. Plates were incubated for 24 hr at 30°C and then imaged. Two biological replicates were performed each in technical triplicate. The β-galactosidase assay was carried out as previously described (**Hammond et al., 2022**). Mixtures of 20 µL of culture, 30 µL of LB, 150 µL Z buffer, 40 µL ONPG (4 mg/mL), 1.9 µL β-mercaptoethanol, and 95 µL polymyxin B (20 mg/mL) were transferred to a 96-well plate and read on a BioTek plate reader. Miller units were then calculated and graphed using GraphPad Prism 9 with the one-way ANOVA and post hoc multiple comparisons.

Immunoblot

Overnight cultures of *S. aureus* cells were back diluted to OD₆₀₀=0.1, grown to midlog phase (OD₆₀₀=0.4), and then induced with 1 mM IPTG and grown for an additional 2 hr. Cells were then standardized to an OD₆₀₀=1.0, lysed with 5 µL lysostaphin (1 mg/mL in 20 mM sodium acetate), and incubated for 30 min at 37°C. 1 µL of DNase A (1 U/µL) was added and incubated for an additional 30 min. Samples were then analyzed by SDS-PAGE analysis, transferred to a membrane, and probed with rabbit antiserum raised against GpsB-GFP. Total protein was visualized from the SDS-PAGE gel using the GelCode Blue Safe Protein Stain (Thermo Fisher, 24596).

Homology model construction of deletion variants

Template-based homology models were made using MODELLER 9.24 (**Eswar et al., 2006**) by constructing 1000 decoys corresponding to each construct based on various template structures.

MD simulations

The GpsB dimers were exposed to conventional MD simulation using Gromacs (v. 5.0.4) (**Abraham et al., 2015; Páll et al., 2014**) with the CHARMM36m force field (**Huang et al., 2017**). Explicit TIP3P water (**Jorgensen et al., 1983**) with 150 mM KCl was used for solvation. A 12 Å cut-off for the van der Waals forces was used. Electrostatic forces were computed using the particle mesh Ewald method (**Darden et al., 1993**). The Verlet cut-off scheme was used. The temperature and pressure were controlled using the Nosé-Hoover (**Nosé, 1984b; Nosé, 1984a; Hoover, 1985; Parrinello**

and Rahman, 1981; Nosé and Klein, 1983) methods, respectively, to sample the NPT ensemble at P=1 bar and T=303.15 K. The integration time step was 2 fs, enabled by using H-bond restraints (Hess et al., 1977). Each system was simulated for 250–500 ns. All systems were made using CHARMM-GUI (Jo et al., 2008; Brooks et al., 2009; Lee et al., 2016).

AlphaFold2 predictions

Prediction of the complex between the GpsB dimer and the C-terminal domain of FtsZ was performed using AlphaFold2 (multimer version 3) (Evans et al., 2021; Varadi et al., 2022) on ColabFold (Mirdita et al., 2022; Steinegger and Söding, 2017). The sequence of GpsB was taken from *S. aureus* (strain COL, UniProt ID: Q5HFX8) and for FtsZ we used *S. aureus* (strain COL, UniProt ID: Q5HGP5) residues 325–390 for the entire C-terminal domain or residues 385–390 for the terminal 6-peptide. Structural predictions were made using all standard options on ColabFold and seeding the template structure resolved in this study between GpsB and the PBP4 fragment (PDB ID: 8E2C) was not observed to improve predictions.

Acknowledgements

We thank Eric Lewandowski for reading the manuscript. We also thank the staff members of the Advanced Photon Source of Argonne National Laboratory, particularly those at the SBC for assistance with X-ray diffraction data collection. SBC-CAT is operated by UChicago Argonne LLC, for the U.S. Department of Energy, Office of Biological and Environmental Research under contract DE-AC02-06CH11357.

Additional information

Funding

Funder	Grant reference number	Author
National Institutes of Health	R21 AI164775	Yu Chen Prahathees Eswara
National Institutes of Health	R35 GM133617	Prahathees Eswara

The funders had no role in study design, data collection and interpretation, or the decision to submit the work for publication.

Author contributions

Michael D Sacco, Conceptualization, Data curation, Formal analysis, Investigation, Visualization, Methodology, Writing - original draft, Writing - review and editing; Lauren R Hammond, Conceptualization, Data curation, Formal analysis, Investigation, Writing - original draft, Writing - review and editing; Radwan E Noor, Dipanwita Bhattacharya, Lily J McKnight, Jesper J Madsen, Xiujun Zhang, Shane G Butler, M Trent Kemp, Aiden C Jaskolka-Brown, Sebastian J Khan, Investigation; Ioannis Gelis, Formal analysis, Investigation, Writing - original draft; Prahathees Eswara, Yu Chen, Conceptualization, Resources, Formal analysis, Supervision, Funding acquisition, Investigation, Methodology, Writing - original draft, Project administration, Writing - review and editing

Author ORCIDs

Michael D Sacco  <http://orcid.org/0000-0001-5930-7363>

Dipanwita Bhattacharya  <http://orcid.org/0000-0002-5000-3846>

Jesper J Madsen  <http://orcid.org/0000-0003-1411-9080>

Prahathees Eswara  <http://orcid.org/0000-0003-4430-261X>

Yu Chen  <http://orcid.org/0000-0002-5115-3600>

Decision letter and Author response

Decision letter <https://doi.org/10.7554/eLife.85579.sa1>

Author response <https://doi.org/10.7554/eLife.85579.sa2>

Additional files

Supplementary files

- Supplementary file 1. Table of crystallographic statistics. *Values in parentheses indicate those for the highest resolution shell.
- Supplementary file 2. Surface plasmon resonance (SPR) dissociation constants (K_D) of *Sa* FtsZ and *Sa* PBP4 derived peptides for *Sa* GpsB^{WT}_{FL} and *Sa* GpsB^{ΔMAD}_{FL}. Concentration response sensorgrams are shown in **Figure 4—figure supplement 2**.
- Supplementary file 3. The genotypes of strains used in the cell-based studies.
- Supplementary file 4. The oligonucleotide and geneblock sequences used in the cell-based studies.
- MDAR checklist

Data availability

All crystal structures have been deposited in the RCSB Protein Data Bank (PDB) with accession IDs of: *Sa* GpsB NTD (PDB ID [8E2B](#)), *Sa* GpsB NTD + *Sa* PBP4 C-term (PDB ID [8E2C](#)).

The following datasets were generated:

Author(s)	Year	Dataset title	Dataset URL	Database and Identifier
Sacco M, Chen Y	2023	N-terminal domain of <i>S. aureus</i> GpsB	https://www.rcsb.org/structure/8E2B	RCSB Protein Data Bank, 8E2B
Sacco M, Chen Y	2023	N-terminal domain of <i>S. aureus</i> GpsB in complex with PBP4 fragment	https://www.rcsb.org/structure/8E2C	RCSB Protein Data Bank, 8E2C

References

- Abraham MJ**, Murtola T, Schulz R, Páll S, Smith JC, Hess B, Lindahl E. 2015. GROMACS: High performance molecular simulations through multi-level parallelism from laptops to supercomputers. *SoftwareX* **1–2**:19–25. DOI: <https://doi.org/10.1016/j.softx.2015.06.001>
- Atilano ML**, Pereira PM, Yates J, Reed P, Veiga H, Pinho MG, Filipe SR. 2010. Teichoic acids are temporal and spatial regulators of peptidoglycan cross-linking in *Staphylococcus aureus*. *PNAS* **107**:18991–18996. DOI: <https://doi.org/10.1073/pnas.1004304107>
- Bartlett TM**, Sisley TA, Mychack A, Walker S, Baker RW, Rudner DZ, Bernhardt TG. 2023. Identification of FacZ as a division site placement factor in *Staphylococcus aureus*. *bioRxiv*. DOI: <https://doi.org/10.1101/2023.04.24.538170>
- Battesti A**, Bouveret E. 2012. The bacterial two-hybrid system based on adenylate cyclase reconstitution in *Escherichia coli*. *Methods* **58**:325–334. DOI: <https://doi.org/10.1016/j.jymeth.2012.07.018>, PMID: 22841567
- Battye TGG**, Kontogiannis L, Johnson O, Powell HR, Leslie AGW. 2011. iMOSFLM: a new graphical interface for diffraction-image processing with MOSFLM. *Acta Crystallographica. Section D, Biological Crystallography* **67**:271–281. DOI: <https://doi.org/10.1107/S0907444910048675>, PMID: 21460445
- Bottomley AL**, Liew ATF, Kusuma KD, Peterson E, Seidel L, Foster SJ, Harry EJ. 2017. Coordination of chromosome segregation and cell division in *Staphylococcus aureus*. *Frontiers in Microbiology* **8**:1575. DOI: <https://doi.org/10.3389/fmicb.2017.01575>, PMID: 28878745
- Brooks BR**, Brooks CL, Mackerell AD, Nilsson L, Petrella RJ, Roux B, Won Y, Archontis G, Bartels C, Boresch S, Cafilisch A, Caves L, Cui Q, Dinner AR, Feig M, Fischer S, Gao J, Hodoscek M, Im W, Kuczera K, et al. 2009. CHARMM: the biomolecular simulation program. *Journal of Computational Chemistry* **30**:1545–1614. DOI: <https://doi.org/10.1002/jcc.21287>, PMID: 19444816
- Brzozowski RS**, White ML, Eswara PJ. 2019. Live-cell fluorescence microscopy to investigate subcellular protein localization and cell morphology changes in bacteria. *Journal of Visualized Experiments* **01**:59905. DOI: <https://doi.org/10.3791/59905>, PMID: 31814606
- Buske PJ**, Levin PA. 2012. Extreme C terminus of bacterial cytoskeletal protein FtsZ plays fundamental role in assembly independent of modulatory proteins. *The Journal of Biological Chemistry* **287**:10945–10957. DOI: <https://doi.org/10.1074/jbc.M111.330324>, PMID: 22298780
- Chatterjee SS**, Chen L, Gilbert A, da Costa TM, Nair V, Datta SK, Kreiswirth BN, Chambers HF. 2017. PBP4 Mediates β -Lactam resistance by altered function. *Antimicrobial Agents and Chemotherapy* **61**:e00932–e00917. DOI: <https://doi.org/10.1128/AAC.00932-17>, PMID: 28807923
- Chen W**, Zhang Y, Yeo WS, Bae T, Ji Q. 2017. Rapid and efficient genome editing in *Staphylococcus aureus* by using an engineered CRISPR/Cas9 System. *Journal of the American Chemical Society* **139**:3790–3795. DOI: <https://doi.org/10.1021/jacs.6b13317>, PMID: 28218837

- Claessen D**, Emmins R, Hamoen LW, Daniel RA, Errington J, Edwards DH. 2008. Control of the cell elongation-division cycle by shuttling of PBP1 protein in *Bacillus subtilis*. *Molecular Microbiology* **68**:1029–1046. DOI: <https://doi.org/10.1111/j.1365-2958.2008.06210.x>, PMID: 18363795
- Cleverley RM**, Rismondo J, Lockhart-Cairns MP, Van Bentum PT, Egan AJF, Vollmer W, Halbedel S, Baldock C, Breukink E, Lewis RJ. 2016. Subunit arrangement in GpsB, a regulator of cell wall biosynthesis. *Microbial Drug Resistance* **22**:446–460. DOI: <https://doi.org/10.1089/mdr.2016.0050>, PMID: 27257764
- Cleverley RM**, Rutter ZJ, Rismondo J, Corona F, Tsui H-CT, Alatawi FA, Daniel RA, Halbedel S, Massidda O, Winkler ME, Lewis RJ. 2019. The cell cycle regulator GpsB functions as cytosolic adaptor for multiple cell wall enzymes. *Nature Communications* **10**:261. DOI: <https://doi.org/10.1038/s41467-018-08056-2>, PMID: 30651563
- Costa SF**, Saraiva BM, Veiga H, Marques LB, Schäper S, Sporniak M, Vega DE, Jorge AM, Duarte AM, Brito AD, Tavares AC, Reed P, Pinho MG. 2023. The Role of GpsB in cell morphogenesis of *Staphylococcus aureus*. *bioRxiv*. DOI: <https://doi.org/10.1101/2023.06.16.545294>
- Darden T**, York D, Pedersen L. 1993. Particle mesh Ewald: An $N \cdot \log(N)$ method for Ewald sums in large systems. *The Journal of Chemical Physics* **98**:10089–10092. DOI: <https://doi.org/10.1063/1.464397>
- Delaglio F**, Grzesiek S, Vuister GW, Zhu G, Pfeifer J, Bax A. 1995. NMRPipe: a multidimensional spectral processing system based on UNIX pipes. *Journal of Biomolecular NMR* **6**:277–293. DOI: <https://doi.org/10.1007/BF00197809>, PMID: 8520220
- Emsley P**, Cowtan K. 2004. Coot: model-building tools for molecular graphics. *Acta Crystallographica. Section D, Biological Crystallography* **60**:2126–2132. DOI: <https://doi.org/10.1107/S0907444904019158>, PMID: 15572765
- Eswar N**, Webb B, Marti-Renom MA, Madhusudhan MS, Eramian D, Shen MY, Pieper U, Sali A. 2006. Comparative protein structure modeling using modeller. *Current Protocols in Bioinformatics* **5**:bi0506s15. DOI: <https://doi.org/10.1002/0471250953.bi0506s15>, PMID: 18428767
- Eswara PJ**, Brzozowski RS, Viola MG, Graham G, Spanoudis C, Trebino C, Jha J, Aubee JI, Thompson KM, Camberg JL, Ramamurthi KS. 2018. An essential *Staphylococcus aureus* cell division protein directly regulates FtsZ dynamics. *eLife* **7**:e38856. DOI: <https://doi.org/10.7554/eLife.38856>, PMID: 30277210
- Evans PR**, Murshudov GN. 2013. How good are my data and what is the resolution? *Acta Crystallographica. Section D, Biological Crystallography* **69**:1204–1214. DOI: <https://doi.org/10.1107/S0907444913000061>, PMID: 23793146
- Evans R**, O'Neill M, Pritzel A, Antropova N, Senior A, Green T, Židek A, Bates R, Blackwell S, Yim J, Ronneberger O, Bodenstern S, Zielinski M, Bridgland A, Potapenko A, Cowie A, Tunyasuvunakool K, Jain R, Clancy E, Kohli P, et al. 2021. Protein complex prediction with alphafold-multimer. *bioRxiv*. DOI: <https://doi.org/10.1101/2021.10.04.463034>
- Farha MA**, Leung A, Sewell EW, D'Elia MA, Allison SE, Ejim L, Pereira PM, Pinho MG, Wright GD, Brown ED. 2013. Inhibition of WTA synthesis blocks the cooperative action of PBPs and sensitizes MRSA to β -lactams. *ACS Chemical Biology* **8**:226–233. DOI: <https://doi.org/10.1021/cb300413m>, PMID: 23062620
- Finan JE**, Archer GL, Pucci MJ, Climo MW. 2001. Role of penicillin-binding protein 4 in expression of vancomycin resistance among clinical isolates of oxacillin-resistant *Staphylococcus aureus*. *Antimicrobial Agents and Chemotherapy* **45**:3070–3075. DOI: <https://doi.org/10.1128/AAC.45.11.3070-3075.2001>
- Fleurie A**, Manuse S, Zhao C, Campo N, Cluzel C, Lavergne J-P, Fretton C, Combet C, Guiral S, Soufi B, Macek B, Kuru E, VanNieuwenhze MS, Brun YV, Di Guilmi A-M, Claverys J-P, Galinier A, Grangeasse C. 2014. Interplay of the serine/threonine-kinase StkP and the paralogs DivIVA and GpsB in pneumococcal cell elongation and division. *PLoS Genetics* **10**:e1004275. DOI: <https://doi.org/10.1371/journal.pgen.1004275>, PMID: 24722178
- Gamba P**, Veening JW, Saunders NJ, Hamoen LW, Daniel RA. 2009. Two-step assembly dynamics of the *Bacillus subtilis* divisome. *Journal of Bacteriology* **191**:4186–4194. DOI: <https://doi.org/10.1128/JB.01758-08>, PMID: 19429628
- Gillaspay AF**. 2006. The *Staphylococcus aureus* NCTC 8325 genome. *Gram-Positive Pathogens* **01**:381–412. DOI: <https://doi.org/10.1128/9781555816513>
- Halbedel S**, Lewis RJ. 2019. Structural basis for interaction of DivIVA/GpsB proteins with their ligands. *Molecular Microbiology* **111**:1404–1415. DOI: <https://doi.org/10.1111/mmi.14244>, PMID: 30887576
- Hammond LR**, White ML, Eswara PJ. 2019. ν IVA la DivIVA! *Journal of Bacteriology* **201**:e00245-19. DOI: <https://doi.org/10.1128/JB.00245-19>, PMID: 31405912
- Hammond LR**, Sacco MD, Khan SJ, Spanoudis C, Hough-Neidig A, Chen Y, Eswara PJ. 2022. GpsB coordinates cell division and cell surface decoration by wall teichoic acids in *Staphylococcus aureus*. *Microbiology Spectrum* **10**:e0141322. DOI: <https://doi.org/10.1128/spectrum.01413-22>
- Hartman BJ**, Tomasz A. 1984. Low-affinity penicillin-binding protein associated with beta-lactam resistance in *Staphylococcus aureus*. *Journal of Bacteriology* **158**:513–516. DOI: <https://doi.org/10.1128/jb.158.2.513-516.1984>, PMID: 6563036
- Henze UU**, Berger-Bächi B. 1995. *Staphylococcus aureus* penicillin-binding protein 4 and intrinsic beta-lactam resistance. *Antimicrobial Agents and Chemotherapy* **39**:2415–2422. DOI: <https://doi.org/10.1128/AAC.39.11.2415>
- Hess B**, Bekker H, Berendsen H, Lincs JF. 1977. A linear constraint solver for molecular simulations. *Journal of Computational Chemistry* **01**:199709. DOI: [https://doi.org/10.1002/\(SICI\)1096-987X\(199709\)1:1<199709::JCC1>3.0.CO;2-1](https://doi.org/10.1002/(SICI)1096-987X(199709)1:1<199709::JCC1>3.0.CO;2-1)
- Hoover WG**. 1985. Canonical dynamics: Equilibrium phase-space distributions. *Physical Review A* **31**:1695–1697. DOI: <https://doi.org/10.1103/PhysRevA.31.1695>
- Huang KH**, Durand-Heredia J, Janakiraman A. 2013. FtsZ ring stability: of bundles, tubules, crosslinks, and curves. *Journal of Bacteriology* **195**:1859–1868. DOI: <https://doi.org/10.1128/JB.02157-12>, PMID: 23457247

- Huang J, Rauscher S, Nawrocki G, Ran T, Feig M, de Groot BL, Grubmüller H, MacKerell AD Jr. 2017. CHARMM36m: an improved force field for folded and intrinsically disordered proteins. *Nature Methods* **14**:71–73. DOI: <https://doi.org/10.1038/nmeth.4067>, PMID: 27819658
- Jo S, Kim T, Iyer VG, Im W. 2008. CHARMM-GUI: a web-based graphical user interface for CHARMM. *Journal of Computational Chemistry* **29**:1859–1865. DOI: <https://doi.org/10.1002/jcc.20945>, PMID: 18351591
- Jorgensen WL, Chandrasekhar J, Madura JD, Impey RW, Klein ML. 1983. Comparison of simple potential functions for simulating liquid water. *The Journal of Chemical Physics* **79**:926–935. DOI: <https://doi.org/10.1063/1.445869>
- Karshikoff A, Nilsson L, Ladenstein R. 2015. Rigidity versus flexibility: the dilemma of understanding protein thermal stability. *The FEBS Journal* **282**:3899–3917. DOI: <https://doi.org/10.1111/febs.13343>, PMID: 26074325
- Kent V. 2024 *White Rose eTheses Online*. University of Sheffield.
- Kocaoglu O, Tsui HCT, Winkler ME, Carlson EE. 2015. Profiling of β -lactam selectivity for penicillin-binding proteins in *Streptococcus pneumoniae* D39. *Antimicrobial Agents and Chemotherapy* **59**:3548–3555. DOI: <https://doi.org/10.1128/AAC.05142-14>, PMID: 25845878
- Korsak D, Markiewicz Z, Gutkind GO, Ayala JA. 2010. Identification of the full set of *Listeria monocytogenes* penicillin-binding proteins and characterization of PBPD2 (Lmo2812). *BMC Microbiology* **10**:239. DOI: <https://doi.org/10.1186/1471-2180-10-239>
- Kunst F, Ogasawara N, Moszer I, Albertini AM, Alloni G, Azevedo V, Bertero MG, Bessières P, Bolotin A, Borchert S, Borriss R, Boursier L, Brans A, Braun M, Brignell SC, Bron S, Brouillet S, Bruschi CV, Caldwell B, Capuano V, et al. 1997. The complete genome sequence of the gram-positive bacterium *Bacillus subtilis*. *Nature* **390**:249–256. DOI: <https://doi.org/10.1038/36786>, PMID: 9384377
- Lee J, Cheng X, Swails JM, Yeom MS, Eastman PK, Lemkul JA, Wei S, Buckner J, Jeong JC, Qi Y, Jo S, Pande VS, Case DA, Brooks CL, MacKerell AD, Klauda JB, Im W. 2016. CHARMM-GUI input generator for NAMD, GROMACS, AMBER, OpenMM, and CHARMM/OpenMM simulations using the CHARMM36 additive force field. *Journal of Chemical Theory and Computation* **12**:405–413. DOI: <https://doi.org/10.1021/acs.jctc.5b00935>, PMID: 26631602
- Leski TA, Tomasz A. 2005. Role of penicillin-binding protein 2 (PBP2) in the antibiotic susceptibility and cell wall cross-linking of *Staphylococcus aureus*: evidence for the cooperative functioning of PBP2, PBP4, and PBP2A. *Journal of Bacteriology* **187**:1815–1824. DOI: <https://doi.org/10.1128/JB.187.5.1815-1824.2005>, PMID: 15716453
- Lutkenhaus J, Pichoff S, Du S. 2012. Bacterial cytokinesis: from z ring to divisome. *Cytoskeleton* **69**:778–790. DOI: <https://doi.org/10.1002/cm.21054>, PMID: 22888013
- Mahone CR, Goley ED. 2020. Bacterial cell division at a glance. *Journal of Cell Science* **133**:jcs237057. DOI: <https://doi.org/10.1242/jcs.237057>, PMID: 32269092
- Maya-Martinez R, Alexander JAN, Otten CF, Ayala I, Vollmer D, Gray J, Bougault CM, Burt A, Laguri C, Fonvielle M, Arthur M, Strynadka NCJ, Vollmer W, Simorre J-P. 2018. Recognition of peptidoglycan fragments by the transpeptidase PBP4 From *Staphylococcus aureus* *Frontiers in Microbiology* **9**:3223. DOI: <https://doi.org/10.3389/fmicb.2018.03223>, PMID: 30713527
- Melander RJ, Zurawski DV, Melander C. 2018. Narrow-spectrum antibacterial agents. *MedChemComm* **9**:12–21. DOI: <https://doi.org/10.1039/C7MD00528H>, PMID: 29527285
- Mirdita M, Schütze K, Moriwaki Y, Heo L, Ovchinnikov S, Steinegger M. 2022. ColabFold: making protein folding accessible to all. *Nature Methods* **19**:679–682. DOI: <https://doi.org/10.1038/s41592-022-01488-1>, PMID: 35637307
- Navratna V, Nadig S, Sood V, Prasad K, Arakere G, Gopal B. 2010. Molecular basis for the role of *Staphylococcus aureus* penicillin binding protein 4 in antimicrobial resistance. *Journal of Bacteriology* **192**:134–144. DOI: <https://doi.org/10.1128/JB.00822-09>, PMID: 19854906
- Nosé S, Klein ML. 1983. Constant pressure molecular dynamics for molecular systems. *Molecular Physics* **50**:1055–1076. DOI: <https://doi.org/10.1080/00268978300102851>
- Nosé S. 1984a. A molecular dynamics method for simulations in the canonical ensemble. *Molecular Physics* **52**:255–268. DOI: <https://doi.org/10.1080/00268978400101201>
- Nosé S. 1984b. A unified formulation of the constant temperature molecular dynamics methods. *The Journal of Chemical Physics* **81**:511–519. DOI: <https://doi.org/10.1063/1.447334>
- Oliva MA, Halbedel S, Freund SM, Dutow P, Leonard TA, Veprintsev DB, Hamoen LW, Löwe J. 2010. Features critical for membrane binding revealed by DivIVA crystal structure. *The EMBO Journal* **29**:1988–2001. DOI: <https://doi.org/10.1038/emboj.2010.99>, PMID: 20502438
- Páll S, Abraham MJ, Kutzner C, Hess B, Lindahl E. 2014. Tackling exascale software challenges in molecular dynamics simulations with GROMACS. International conference on exascale applications and software. 3–27. DOI: <https://doi.org/10.1007/978-3-319-15976-8>
- Parrinello M, Rahman A. 1981. Polymorphic transitions in single crystals: a new molecular dynamics method. *Journal of Applied Physics* **52**:7182–7190. DOI: <https://doi.org/10.1063/1.328693>
- Reichmann NT, Tavares AC, Saraiva BM, Jousselin A, Reed P, Pereira AR, Monteiro JM, Sobral RG, VanNieuwenhze MS, Fernandes F, Pinho MG. 2019. SEDS-bPBP pairs direct lateral and septal peptidoglycan synthesis in *Staphylococcus aureus*. *Nature Microbiology* **4**:1368–1377. DOI: <https://doi.org/10.1038/s41564-019-0437-2>, PMID: 31086309
- Rismondo J, Cleverley RM, Lane HV, Großhennig S, Steglich A, Möller L, Mannala GK, Hain T, Lewis RJ, Halbedel S. 2016. Structure of the bacterial cell division determinant GpsB and its interaction with penicillin-

- binding proteins. *Molecular Microbiology* **99**:978–998. DOI: <https://doi.org/10.1111/mmi.13279>, PMID: 26575090
- Santiago M**, Matano LM, Moussa SH, Gilmore MS, Walker S, Meredith TC. 2015. A new platform for ultra-high density *Staphylococcus aureus* transposon libraries. *BMC Genomics* **16**:252. DOI: <https://doi.org/10.1186/s12864-015-1361-3>, PMID: 25888466
- Singh JK**, Makde RD, Kumar V, Panda D. 2007. A membrane protein, EzrA, regulates assembly dynamics of FtsZ by interacting with the C-terminal tail of FtsZ. *Biochemistry* **46**:11013–11022. DOI: <https://doi.org/10.1021/bi700710j>, PMID: 17718511
- Snowden MA**, Perkins HR. 1990. Peptidoglycan cross-linking in *Staphylococcus aureus*: an apparent random polymerisation process. *J European Journal of Biochemistry* **191**:373–377. DOI: <https://doi.org/10.1111/j.1432-1033.1990.tb19132.x>
- Steele VR**, Bottomley AL, Garcia-Lara J, Kasturiarachchi J, Foster SJ. 2011. Multiple essential roles for EzrA in cell division of *Staphylococcus aureus*. *Molecular Microbiology* **80**:542–555. DOI: <https://doi.org/10.1111/j.1365-2958.2011.07591.x>, PMID: 21401734
- Steinegger M**, Söding J. 2017. MMseqs2 enables sensitive protein sequence searching for the analysis of massive data sets. *Nature Biotechnology* **35**:1026–1028. DOI: <https://doi.org/10.1038/nbt.3988>, PMID: 29035372
- Sutton JAF**, Cooke M, Tinajero-Trejo M, Wacnik K, Salamaga B, Portman-Ross C, Lund VA, Hobbs JK, Foster SJ. 2023. The roles of GpsB and DivIVA in *Staphylococcus aureus* growth and division. *Frontiers in Microbiology* **14**:1241249. DOI: <https://doi.org/10.3389/fmicb.2023.1241249>, PMID: 37711690
- Tavares JR**, de Souza RF, Meira GLS, Gueiros-Filho FJ. 2008. Cytological characterization of YpsB, a novel component of the *Bacillus subtilis* divisome. *Journal of Bacteriology* **190**:7096–7107. DOI: <https://doi.org/10.1128/JB.00064-08>, PMID: 18776011
- Vagin A**, Lebedev A. 2024. *Acta Crystallographica A-Foundation and Advances*. Foundation and Advances.
- Varadi M**, Anyango S, Deshpande M, Nair S, Natassia C, Yordanova G, Yuan D, Stroe O, Wood G, Laydon A, Židek A, Green T, Tunyasuvunakool K, Petersen S, Jumper J, Clancy E, Green R, Vora A, Lutfi M, Figurnov M, et al. 2022. AlphaFold protein structure database: massively expanding the structural coverage of protein-sequence space with high-accuracy models. *Nucleic Acids Research* **50**:D439–D444. DOI: <https://doi.org/10.1093/nar/gkab1061>, PMID: 34791371
- Wyke AW**, Ward JB, Hayes MV, Curtis NA. 1981. A role in vivo for penicillin-binding protein-4 of *Staphylococcus aureus*. *European Journal of Biochemistry* **119**:389–393. DOI: <https://doi.org/10.1111/j.1432-1033.1981.tb05620.x>, PMID: 7308191